Turun yliopisto
University of Turku

THE ROLE OF STRUCTURAL IMPERFECTIONS IN Sr_2FeMoO_6 THIN FILMS

Minnamari Saloaro
née Metsänoja

TURUN YLIOPISTON JULKAISUJA – ANNALES UNIVERSITATIS TURKUENSIS
Sarja - ser. AI osa - tom. 527 | Astronomica - Chemica - Physica - Mathematica | Turku 2015

University of Turku

Faculty of Mathematics and Natural Sciences
Department of Physics and Astronomy
Wihuri Physical Laboratory

Supervised by

Prof. Petriina Paturi
Wihuri Physical Laboratory
Dept. of Physics and Astronomy
University of Turku
Turku, Finland

Dr. Hannu Huhtinen
Wihuri Physical Laboratory
Dept. of Physics and Astronomy
University of Turku
Turku, Finland

Dr. Sayani Majumdar
NanoSpin
Dept. of Applied Physics
Aalto University School of Science
Espoo, Finland

Reviewed by

Prof. Sebastiaan van Dijken
NanoSpin
Dept. of Applied Physics
Aalto University School of Science
Espoo, Finland

Dr. Roland Mathieu
Solid State Physics
Dept. of Engineering Sciences
Uppsala University
Uppsala, Sweden

Opponent

Prof. Michael Lorenz
Halbleiterphysik
Institut für Experimentelle Physik II
Universität Leipzig
Leipzig, Germany

The originality of this thesis has been checked in accordance with the University of Turku quality assurance system using the Turnitin OriginalityCheck service.

ISBN 978-951-29-6308-9 (PRINT)
ISBN 978-951-29-6309-6 (PDF)
ISSN 0082-7002
Painosalama Oy - Turku, Finland 2015

Preface

Acknowledgments

This work has been carried out in the Wihuri Physical Laboratory of the Department of Physics and Astronomy at University of Turku. The Jenny and Antti Wihuri Foundation, the Magnus Ehrnrooth Foundation and the University of Turku Graduate School's Doctoral Program in Physical and Chemical Sciences are acknowledged for financial support.

I appreciate the helpful comments and the time Prof. Sebastiaan van Dijken and Dr. Roland Mathieu spent carefully reviewing my thesis. I would like to thank Prof. Michael Lorenz, it is an honor to have you as my opponent. I express my sincere gratitude to Prof. Petriina Paturi for the bright supervision that has provided great opportunities and confidence to find my way in physics. Her efforts and the time she always finds for us students are invaluable. The endless discussions about physics and beyond with Dr. Hannu Huhtinen have been more than precious and I am deeply grateful for his kind and inventive guidance. The deep knowledge of Dr. Sayani Majumdar on the magnetism has been an amazing asset and I really appreciate our creative discussions.

I have no words to really express my gratitude to my colleague Dr. Heikki Palonen for all the help, explanations and support I have received since the first day at the university. I would like to thank my colleague MSc Mika Malmivirta for the patient listening and infinite willingness to help. Also, all the current and former colleagues in our research group at the Wihuri Physical Laboratory deserve many thanks. Although, I do not have the space to individually thank each of you, I am truly grateful for everything, especially making even the most frustrating days enjoyable.

I would like to thank our collaborators in Halle, especially Prof. Wolfram Hergert, Dr. Arthur Ernst and MSc Martin Hoffmann. Also, Prof. Kalevi Kokko is thanked for enabling this great collaboration. Dr. Hakan Deniz and Prof. Dietrich Hesse are acknowledged for all their efforts with the TEM images. Dr. Sari Granroth is deeply appreciated for her patient explanations as well as the excellent collaboration and support. Also, the efforts of Dr. Pekka Laukkanen with the SFMO samples are highly valued.

I consider myself very lucky because I have come across so many amazing people during the years at the University and even before whom I can nowadays call friends. All the shared moments with laughter and sorrow have been priceless, and I could not

have come this far without you. I am heartily grateful for my mother's never ending faith in me, my father's realistic view and support as well as my brother's enthusiasm towards the things I do. I greatly value the support of my grandparents, my in-laws and my godfather's family. I am happy that you all are in my life.

Finally, I wish to thank my loving husband Mikko. You have kept me sane during the endless hours with this thesis, have made me believe in myself even at the moments when I felt like giving up and most importantly, have been there for me, always.

Turku, November 2015

Minnamari Saloaro

Abstract

In this work, Sr_2FeMoO_6 (SFMO) thin films were studied with the main focus on their magnetic and magneto-transport properties. The fabrication process of pulsed laser deposited SFMO films was first optimized. Then the effects of strain, film thickness and substrate were thoroughly investigated. In addition to these external factors, the effect of intrinsic defects on the magnetic properties of SFMO were also clarified. Secondly, the magnetoresistivity mechanims of SFMO films were studied and a semiempirical model of the temperature dependence of resistivity was introduced.

The films were grown on single crystal substrates using a ceramic target made with sol-gel method. The structural characterization of the films were carried out with X-ray diffraction, atomic force microscopy, transmission electron microscopy and high kinetic energy photoelectron spectroscopy. The magnetic properties were measured with SQUID magnetometer and the magneto-transport properties by magnetometer with a resistivity option.

SFMO films with the best combination of structural and magnetic properties were grown in Ar atmosphere at 1050 °C. Their magnetic properties could not be improved by the *ex situ* post-annealing treatments aside from the treatments in ultra-high vacuum conditions. The optimal film thickness was found to be around 150 nm and only small improvement in the magnetic properties with decreasing strain was observed. Instead, the magnetic properties were observed to be highly dependent on the choice of the substrate due to the lattice mismatch induced defects, which are best avoided by using the $SrTiO_3$ substrate. The large difference in the Curie temperature and the saturation magnetization between the SFMO thin film and polycrystalline bulk samples was connected to the antisite disorder and oxygen vacancies. Thus, the Curie temperature of SFMO thin films could be improved by increasing the amount of oxygen vacancies for example with ultra-high vacuum treatments or improving the B-site ordering by further optimization of the deposition parameters.

The magneto-transport properties of SFMO thin films do not follow any conventional models, but the temperature dependence of resistivity was succesfully described with a model of two spin channel system. Also, evidences that the resistivity-temperature behaviour of SFMO thin films is dominated by the structural defects, which reduce the band gap in the majority spin band were found. Moreover, the magnetic field response of the resistivity in SFMO thin films were found to be superposition of different mechanisms that seems to be related to the structural changes in the film.

Tiivistelmä

Tässä työssä keskityttiin Sr_2FeMoO_6 (SFMO) ohutkalvojen tutkimukseen pääpainon ollessa niiden magneettisissa ominaisuuksissa ja magneettikentästä riippuvissa virrankuljetusominaisuuksissa. Laserhöyrystyksellä tehtyjen SFMO ohutkalvojen valmistusprosessi optimoitiin, jonka jälkeen venytyksen, kalvon paksuuden ja kasvatusalustan vaikutus tutkittiin huolellisesti. Näiden ulkoisten tekijöiden lisäksi, kalvon sisäisten virheiden vaikutusta sen magneettisiin ominaisuuksiin selvennettiin. Toisaalta työssä tarkasteltiin myös SFMO ohutkalvojen magnetoresistiivisyysominaisuuksia ja esiteltiin puoliempiirinen malli resistiivisyyden lämpötilariippuvuudelle.

SFMO kalvot kasvatettiin yksittäiskidealustoille käyttäen sooli-geeli menetelmällä valmistettua keraamista kohtiota. Rakenteellinen karakterisointi suoritettiin röntgendiffraktiolla, atomivoimamikroskopialla, läpäisyelektronimikroskopialla ja korkean kineettisen energian fotoelektronispektroskopialla. Magneettiset ominaisuudet mitattiin SQUID-magnetometrillä ja virrankuljetus ominaisuudet magneettikentässä magnetometrillä, jossa on resistiivisyys optio.

Parhaat SFMO ohutkalvot kasvatettiin Ar kaasukehässä 1050 °C lämpötilassa. Niiden magneettisia ominaisuuksia ei kyetty parantamaan kasvatuksen jälkeisillä lämpökäsittelyillä lukuunottamatta käsittelyä ultravakuumiolosuhteissa. Optimaaliseksi kalvon paksuudeksi saatiin noin 150 nm ja venymän havaittiin vaikuttavan magneettisiin ominaisuuksiin vain vähän. Sen sijaan, magneettisten ominaisuuksien havaittiin olevan vahvasti riippuvaisia kasvatusalustasta hilojen yhteensopimattomuuden aiheuttamien kidevirheiden takia, jotka voidaan parhaiten välttää käyttämällä $SrTiO_3$ alustaa. Ohutkalvojen ja monikiteisten bulkki näytteiden välillä olevan suuren eron Curien lämpötilassa ja saturaatiomagnetisaatiossa havaittiin liittyvän Fe/Mo-epäjärjestyksen ja happivakanssien määrään. Näin ollen SFMO ohutkalvojen Curien lämpötilaa voidaan parantaa kasvattamalla happivakanssien määrää esimerkiksi ultravakuumikäsittelyllä tai parantamalla Fe/Mo-järjestystä optimoimalla kasvatusparametrejä edelleen.

SFMO ohutkalvojen magneettikentästä riippuvat virrankuljetusominaisuudet eivät noudata mitään tunnettua mallia, mutta resisitiivisyyden lämpötilariippuvuutta kuvattiin onnistuneesti työssä kehitetyllä kahden spinkanavan mallilla. Lisäksi löydettiin näyttöä siitä, että energia-aukkoa enemmistö spinvyössä pienentävät virheet dominoivat resistiivisyyden lämpötilariippuvuutta SFMO ohutkalvoissa. Magnetoresistiivisyyden SFMO ohutkalvoissa havaittiin taas olevan yhdistelmä useita eri mekanismeja, jotka vaikuttavat olevan kytköksissä kalvojen rakenteellisiin muutoksiin.

Articles included in this thesis

This thesis is based on the experimental work carried out at the Wihuri Physical Laboratory, Department of Physics and Astronomy, University of Turku during the years 2011 – 2015. The thesis consists of an introductory part and of the following publications:

[**P1**] P. Paturi, M. Metsänoja and H. Huhtinen: *Optimization of the deposition temperature and atmosphere for pulsed laser deposited* Sr_2FeMoO_6 *thin films*, Thin Solid Films **519**, 8047 (2011).

[**P2**] M. Metsänoja, S. Majumdar, H. Huhtinen and P. Paturi: *Effect of ex situ post-annealing treatments on* Sr_2FeMoO_6 *thin films*, Journal of Superconductivity and Novel Magnetism **25**, 829 (2012).

[**P3**] M. Saloaro, S. Majumdar, H. Huhtinen and P. Paturi: *Absence of traditional magnetoresistivity mechanisms in* Sr_2FeMoO_6 *thin films grown on* $SrTiO_3$*, MgO and* $NdGaO_3$ *substrates*, Journal of Physics: Condensed Matter **24**, 366003 (2012).

[**P4**] M. Saloaro, S. Majumdar, H. Huhtinen and P. Paturi: *The effect of film thickness on the magnetic and magneto-transport properties of* Sr_2FeMoO_6 *thin films*, EPJ Web of Conferences **40**, 15012 (2013).

[**P5**] M. Saloaro, H. Deniz, H. Huhtinen, H. Palonen, S. Majumdar and P. Paturi: *The predominance of substrate induced defects in magnetic properties of* Sr_2FeMoO_6 *thin films*, Journal of Physics: Condensed Matter **27**, 386001 (2015).

[**P6**] M. Saloaro, M. Hoffmann, W. A. Adeagbo, S. Granroth, H. Deniz, H. Palonen, H. Huhtinen, S. Majumdar, P. Laukkanen, W. Hergert, A. Ernst and P. Paturi: *Towards high Curie temperatures in* Sr_2FeMoO_6 *thin films*, Advanced Materials (submitted).

Articles relevant to this work but not included in this thesis

[**P7**] I. Angervo, M. Saloaro, H. Palonen, S. Majumdar, H. Huhtinen and P. Paturi: *Thickness dependent properties of* Sr_2FeMoO_6 *thin films grown on* $SrTiO_3$ *and* $(LaAlO_3)_{0.3}(Sr_2AlTaO_6)_{0.7}$ *substrates*, Physics Procedia (in print).

Contents

1 Introduction

1.1 Motivation

Spintronics has been an emerging field since the discovery of the GMR effect in 1988. It is hoped to be a solution for the continuously growing need for faster data processing and larger data storage capacity, for which the conventional semiconductor based electronics might not be able to match in the future. When the spin degree of freedom is taken into use, high potential in nonvolatility, increased data processing speed and integration densities as well as energy saving arises. The existing spintronic applications like the GMR read heads in hard disc drives and the magnetic random access memories have already proven the advantages of the spintronic devices and ensured the spintronics place as a part of the future electronics.

Spintronic components are basically multilayer structures and their operation is highly dependent on the properties of the used materials. Therefore, the material research focused on high quality thin films is a central part in the development and advancement of the spintronic devices. There are wide variety of potential materials from magnetic semiconductors to complex magnetic oxides and one of them is the Sr_2FeMoO_6 (SFMO). With relatively high Curie temperature, SFMO has large intrinsic magnetoresistance and high spin polarization even at room temperature. These increase its possibilities in novel devices even though SFMO cannot compete with metallic ferromagnetic materials in conventional spintronic structures. In addition, the fabrication of SFMO is quite demanding due to easily formed impurity phases and defects. The thin film fabrication requires rather high temperatures and well controlled atmosphere with low pressure. Therefore, reasonably good SFMO films have been fabricated only in recent years. Nevertheless, the magnetic properties desired for these applications have been weaker in SFMO thin films compared with polycrystalline materials. Hence, one aspect of the SFMO research is to clarify the mechanisms that affect the magnetic properties and are behind the changes between the films and polycrystalline bulk samples. On the other hand, no explanation has been provided for the interesting magnetoresistive phenomena in SFMO thin films that potentially increase its usability in magnetoresistive sensor applications. The fundamental understanding of the magnetotransport mechanisms in SFMO thin films is the other aspect of the SFMO research. All in all, the ongoing SFMO investigations are focused on the optimization of the SFMO films for the further research related to SFMO based multilayer structures, which could be used in these applications.

The potential applications are inevitably one of the motivating factors in this work, but the fundamental scientific understanding of the magnetic and magnetotransport mechanisms is at least as important. To increase the understanding of this intriguing material and to optimize the films towards novel applications, the magnetic and magnetoresistive properties of SFMO thin films with various structural imperfections will be discussed in this work. At the beginning of this thesis some basic concepts of magnetism and magnetic materials as well as basic properties of SFMO are introduced. Thereafter, the used experimental methods are presented. The first part of this thesis related to the results is focused on the optimization of the deposition process of SFMO thin films, which is an important starting point for following investigations. The second and third parts deal with the substrate and film thickness related changes in the magnetic properties of SFMO films, concentrating on the effect of strain and lattice mismatch induced changes, which are unavoidable in thin films. The focus of the fourth part is in the intrinsic properties of the SFMO, which, on the other hand, are behind the differences between the thin films and bulk samples. Each of these sections is focused on certain structural imperfections in SFMO with minimizing the contribution of other defects. However, the effect of other imperfections can never be totally eliminated in experiments with real samples. Finally, the last part of this thesis concentrates on the magneto-transport properties of SFMO thin films.

1.2 Magnetic ordering

Magnetic behaviour of a material is highly dependent on the orientation of its magnetic moments at the atomic lattice sites. Each of these magnetic moments originates from electronic spins, electronic orbital motion around the nucleus and change in the orbital motion by an applied magnetic field. The nucleus has also a magnetic moment, but it is three orders of magnitude smaller than those associated with the electrons and therefore, it can often be neglected. The change of the orbital motion in applied magnetic field gives the diamagnetic contribution to the magnetization, M, which is the magnetic moment per unit volume. The magnetic susceptibility, $\chi = M/H$, where H is the applied field, is usually weak for diamagnets and their negative susceptibility is often outshined by the positive paramagnetic susceptibility. However, in the materials with filled electron shells, the spin and orbital moment are zero and the only contribution to the magnetization is diamagnetic.

In addition to the paramagnetic disorder, the magnetic moments in materials with unfilled electron shells can be ferro-, antiferro- or ferrimagnetically ordered. A simple

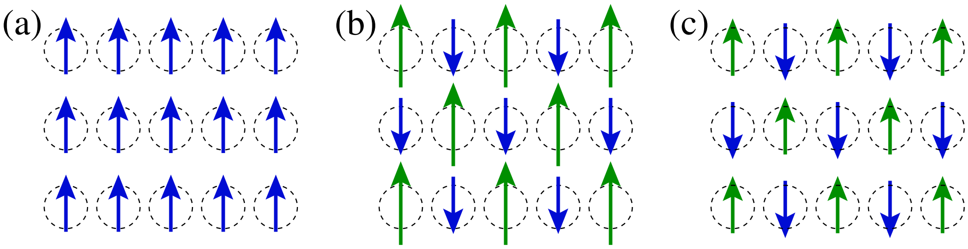

Figure 1. Simplified model of the (a) ferromagnetic, (b) ferrimagnetic and (c) antiferromagnetic orders.

model of the magnetic orders is illustrated in figure 1. A special feature of the ferromagnet is the spontaneous magnetization *i.e.* it has magnetic moment without external magnetic field. The existence of the spontaneous magnetization and the ferromagnetism was modeled by Pierre Weiss in 1906 with the molecular field theory. The theory is based on an internal molecular field that acts on each magnetic moment and is proportional to the magnetization. Thus the internal field that each magnetic moment experiences, is $H_\mathrm{i} = \lambda M + H$, where λ is the Weiss coefficient [1, p. 129]. The magnetization of a ferromagnet is obtained, when H_i is introduced to the Brillouin theory of the paramagnets by replacing the external magnetic field in the Brillouin function. Due to the molecular field, λM, the magnetization is non-zero in zero applied field and the spontaneous magnetization exists. Even though the molecular field is not real, it is a fairly good approximation of the quantum mechanical exchange interaction and it can be used to derive the Curie-Weiss law [2, p. 324]

$$\chi = \frac{C}{T - T_\mathrm{C}}, \tag{1}$$

where the C is the Curie constant, T is the absolute temperature and $T_\mathrm{C} = C\lambda$ is the Curie temperature. The Curie-Weiss law is used to describe the susceptibility in the paramagnetic region above the Curie temperature where the ferromagnetic ordering is lost. The ferrimagnets also possess spontaneous magnetization, but they follow the Curie-Weiss law only at very high temperatures [3, p. 11].

When the ferro- or ferrimagnet is exposed to an increasing external magnetic field, the magnetization increases reversibly until a critical field value is reached. Above that the magnetization is not reversible and a hysteresis is formed. The hysteresis behaviour is caused by the domain structure, which means that the ferro- or ferrimagnetic material is divided into a uniformly magnetized regions. These domains are separated by domain walls, in which the magnetization rotates from one easy direction to another, usually 90° or 180°. The external magnetic field causes the domain wall movement and the rotation of the magnetization inside domains towards the field direction, which is seen as a change in the net magnetization of the material [1, p. 240].

Magnetic ordering results from the exchange interaction between the magnetic moments of the material. The interaction between two localized spins, which are close enough that their wave functions overlap, can be described with the Heisenberg model

$$\mathscr{H} = -\sum_{i<j} J_{ij} S_i \cdot S_j, \tag{2}$$

where the coupling constant, J_{ij}, is positive for parallel spins (ferromagnetic) and negative for antiparallel spins (antiferro- and ferrimagnetic) [4, p. 288]. This direct exchange interaction couples the atomic spins as seen in the equation (2). Therefore, it can only be applied to materials for which the spin, S, is a good quantum number, as occurs in the $3d$ transition metals [1, p. 138].

The magnetic ordering of many magnetic oxides and similar materials can not be explained with the direct exchange interaction. Even though the electrons are localized, the magnetic moments can be located too far apart or separated with a nonmagnetic ion so that they can not directly interact with one another. In the superexchange interaction, the spins of two magnetic ions are coupled indirectly through the intermediate nonmagnetic ion. The antiferromagnetic superexchange interaction between two Mn^{3+}-ions is presented in figure 2(a). The $3d$-orbital of the Mn^{3+}-ion overlaps with $2p$-orbital of the O^{2-}-ion forming a covalent bond. Due to the Pauli exclusion principle, the $2p$-electrons of oxygen ions have to have opposite spins. Also, the spin of the $3d$-electron has to be opposite to the $2p$-electron spin to which it is covalently bonded. As a result, the $3d$-electron spins in Mn^{3+}-ion are in opposite direction when compared to the $3d$-electron spins in the next Mn^{3+}-ion and hence the antiferromagnetic ordering is formed. The $3d$-orbital of the Mn-ion is split into t_{2g}- and e_g-orbitals due to the crystal field. Because of their orientation, the e_g-orbitals have a larger overlap with the $2p$-orbitals and the e_g-electrons are involved in the bonds. The superexchange interaction can also be ferromagnetic if the bond angle between the magnetic ion and the nonmagnetic ion is ∼90° or the interaction is from half-filled to an empty orbital or from a filled to a half-filled orbital [1, p. 139]. The ferromagnetic superexchange interaction is weak and less common than the antiferromagnetic superexchange interaction.

In case the material has both localized and delocalized d-electrons, the magnetic exchange can be explained with the double exchange interaction. The double exchange interaction also occurs between two magnetic ions separated with a nonmagnetic ion. However, the double exchange is mediated with an electron moving from one magnetic ion to another through the nonmagnetic ion. A schematic illustration of the double exchange interaction between Mn^{3+} and Mn^{4+}-ions is shown in figure 2(b). The e_g-electron from the Mn^{3+} moves to the O^{2-}-ion and simultaneously electron moves from O^{2-}-ion to the Mn^{4+}. The Pauli exclusion principle requires that the electrons moving to and from the O^{2-}-ion have to have parallel spins. Also, the spin of the e_g-electron has to be parallel with the spins of the t_{2g}-electrons due to the Hund's rules. Therefore, the $3d$-electron spins of the Mn^{3+} and Mn^{4+} are parallel, which leads to a ferromagnetic ordering.

1.3 Spin transport and magnetoresistance

The resistivity of a normal metal consists of the temperature independent part arising from the impurities and defects, ρ_0, as well as the temperature dependent part from the phonon scattering $\rho_p(T)$, which is proportional to T^n. At high temperatures well above the Debye temperature, where all the lattice waves are excited, the $n = 1$ and below the Debye temperature, the $n = 5$ [4, p. 205]. Also, other scattering mechanisms may have notable contribution in the metallic resistivity like the electron-electron scattering, which has T^2 dependence [5]. Ferromagnetic metals have also a temperature dependent contribution from the scattering related to the magnetic order, $\rho_m(T)$. According to the Matthiessen's rule, the total resistivity is simply a sum of all the individual resistivities present in the sample.

The resistance of ferromagnetic metals can be described with a Mott's two-current model [6, 7], in which the electron scattering from impurities is different for majority (spin up) and minority (spin down) electrons. This results in two independent conduction channels connected in parallel. The corresponding resistivities, $\rho_\uparrow$ and $\rho_\downarrow$, of the spin-up and spin-down conduction channels give the total resistivity, which can be expressed as [4, p. 216]

$$\rho = \frac{\rho_\uparrow \rho_\downarrow}{\rho_\uparrow + \rho_\downarrow}. \tag{3}$$

However, the Mott's two-current model neglects the spin-flip scattering. When the resistivity, $\rho_{\uparrow\downarrow}$, that describes the spin-flip rate, is taken into account, the total resistivity can be expressed as [8]

$$\rho = \frac{\rho_\uparrow \rho_\downarrow + \rho_{\uparrow\downarrow}(\rho_\uparrow + \rho_\downarrow)}{\rho_\uparrow + \rho_\downarrow + 4\rho_{\uparrow\downarrow}}. \tag{4}$$

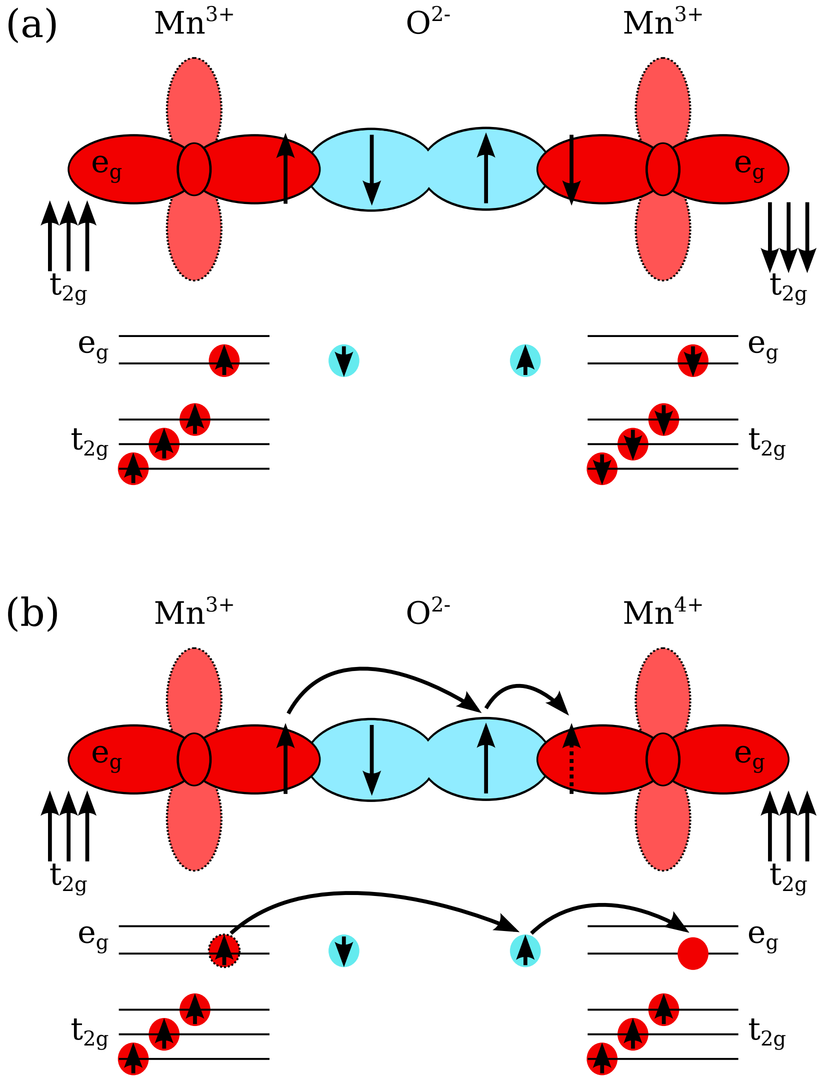

Figure 2. Schematic illustration of (a) the antiferromagnetic superexchange interaction between two Mn^{3+}-ions separated with a nonmagnetic O^{2-}-ion and (b) the double exchange interaction in a Mn^{3+}-O^{2-}-Mn^{4+} chain.

At low temperatures the $\rho_{\uparrow\downarrow}$ is zero and this equation reduces to (3), but at temperatures above T_C it has to be taken into account [1, p. 184].

Magnetoresistance (MR) is a phenomenon where the resistance of a material is dependent on the applied magnetic field strength and it can be described by [1, p. 84]

$$\mathrm{MR}(\%) = \frac{R_B - R_0}{R_0} \times 100, \tag{5}$$

where the R_B is the resistance in applied field and the R_0 is the zero-field resistance. The MR effect can be an intrinsic property of the material like the anisotropic magnetoresistance (AMR) and the colossal magnetoresistance (CMR) or it can be observed in certain multilayer structures like in case of the giant magnetoresistance (GMR).

The MR in normal metals is caused by the cyclotron motion of the electrons in magnetic field, which reduces the electron's mean free path. This is called the ordinary magnetoresistance (OMR) and it is often proportional to the B^2 [4, p. 212]. The effect is very weak when the field and the current are parallel, but notably larger when the field is perpendicular to the current. Similar phenomenon called anisotropic magnetoresistance (AMR) is observed in ferromagnetic metals, where the resistivity depends on the angle between the current and the magnetization.

Large change in resistance with applied field can be achieved with multilayer structure of ferromagnetic (FM) layers coupled antiferromagnetically through conductive non-magnetic (NM) spacer layers and it is called giant magnetoresistance (GMR). The sign of the exchange coupling in these multilayers oscillates with the spacer layer thickness as the RKKY interaction, which means that the interlayer coupling could also be ferromagnetic or zero depending on the thickness of the spacer layer [1, p. 280]. The GMR was first observed in Fe/Cr multilayer structures and the discovery soon led to the commercial applications like magnetic field sensors used in hard disk drives [9, 10]. The giant decrease in resistance under applied field can be explained with the Mott's two current model, which assumes two parallel connected spin channels. Figure 3 shows a schematic picture of the current flow in the GMR structure according to this model. In the low resistance state, the FM layers are parallel and the scattering of the spin up electrons is weaker than the scattering of the spin down electrons through the whole GMR structure. Then, the resistance of the spin up channel through the whole layer structure is low. In the high resistance state (without an applied field), the FM layers are antiparallel and the scattering of spin up electrons is weak in one FM layer and strong in the other. The situation is opposite for the spin down electrons. In this case the resistance is large for the spin up channel through the first FM layer and for the spin down channel

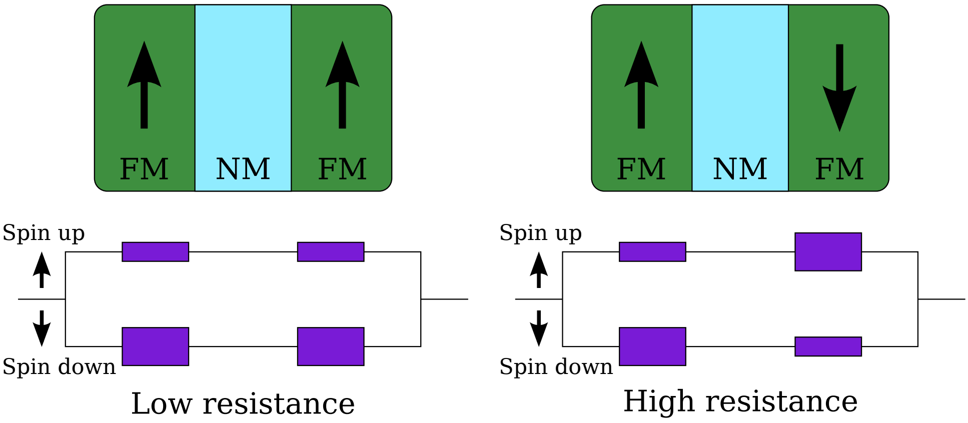

Figure 3. The GMR multilayer structure in low and high resistance state. The schematic electric circuits represent the resistance of the two separate spin channels in the FM layers.

through the second FM layer resulting a giant change in the overall resistance of the GMR structure. However, this model does not take into account the interface scattering that occurs between the FM and NM layers, which is often dominant effect in multilayer structures [11–13].

Tunneling magnetoresistance (TMR) is also observed in some multilayer structures, where the ferromagnetic layers are separated by a thin insulating layer instead of the conductive non-magnetic layer. When the insulating layer is thin enough, the electrons can tunnel from one ferromagnetic layer to another. The resistance of the TMR structure depends on the orientation of the magnetization in the ferromagnetic layers having corresponding high and low resistance states as the GMR structure. The tunneling magnetoresistance also depends on the spin polarization of the charge carriers in the ferromagnetic layers, which can be expressed with Julliere's formula [14]

$$\mathrm{TMR} = \frac{2P_1P_2}{1+P_1P_2}, \tag{6}$$

where the P_1 and P_2 are the spin polarizations of the ferromagnetic layers. The formula is still widely used, even though it is a crude approximation that only takes into account the density of states at the Fermi level.

Unlike the GMR, orders of magnitude greater MR effect called colossal magnetoresistance (CMR) is an intrinsic property of certain materials. The CMR is usually found in 3*d* transition metal oxides like manganites and it is associated with the ferro-paramagnetic phase transition [15]. The physical origin of the CMR phenomena has not been fully explained, but the electron hopping in the double exchange materials and the phase separation have been considered [1, 16]. Below T_C the antiferromagnetic insulating phase competes with the ferromagnetic phase, which is mediated by the double exchange mechanism. Thus, the antiferromagnetic clusters coexist with the FM clusters in CMR materials. When an external field is applied, the magnetic moments are aligned. This promotes electron hopping in the ferromagnetic phase and enhances the double exchange interaction.

1.4 Sr_2FeMoO_6

Strontium iron molybdenum oxide, Sr_2FeMoO_6 (SFMO), has drawn plenty of interest after Kobayashi *et al.* discovered its room-temperature magnetoresistance in 1998 [17]. The discovery revealed that SFMO is an attractive material for spintronic and magnetoresistive applications and lead to ongoing research towards high quality thin films.

The structure of SFMO is ordered double perovskite $A_2BB'O_6$ (figure 4(a)), where A is an alkali earth metal, B (Fe) and B' (Mo) are heterovalent transition metals. The Fe and Mo atoms are positioned inside an oxygen octahedron and they alternate in the structure. Inside the cube formed by these octahedra are the Sr atoms (figure 4(c). The crystal structure of the ideal SFMO is tetragonal and the unit cell is visualized in figure 4(b). According to the X-ray diffraction studies, the space group of SFMO is either I4/m [18] or I4/mmm [19]. Depending on Fe/Mo stoichiometry and ordering, SFMO can also adopt cubic $Fm\bar{3}m$ structure [20–22]. The lattice parameters observed for SFMO sintered bulk and powder samples are around $a = b = 5.58\,\text{Å}$ and $c = 7.90\,\text{Å}$ [23, 24]. In SFMO thin films, the lattice parameters are affected by the changes in the deposition parameters and the strain caused by the substrate [23, 25–30].

Instead of the optimal ordering, it is possible that the Fe atoms and the Mo atoms are transposed in the SFMO structure. This crystal imperfection is called anti-site disorder (ASD), B-site disorder or mis-site defect. In addition to a point defect, the mis-placed Fe atoms can form rows called antiphase boundaries (APB), which act as a barrier for the current and form domain walls [31]. The optimal SFMO structure and the structure involving ASD or APB are schematically illustrated in figure 5(a)-(c). Other defects like oxygen vacancies are also possible in SFMO and it is impossible to grow defect free SFMO sintered bulk, single crystal or thin film samples [32]. The effect of ASD and oxygen vacancies on the magnetic and transport properties of the SFMO has been shown both experimentally and theoretically [32–36]. The reduction of the half metallic feature due to these defects has also been confirmed in many theoretical studies [36–40].

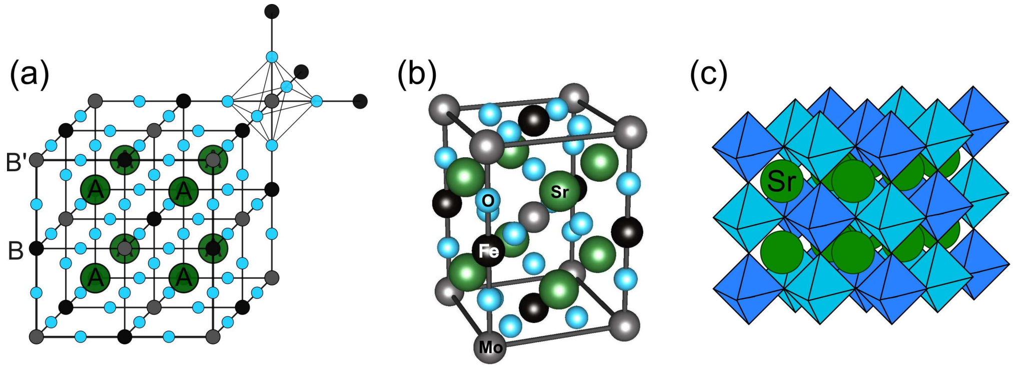

Figure 4. (a) Double perovskite $A_2BB'O_6$ structure. The Sr atoms are on site A, the Fe atoms are on site B and the Mo atoms are on site B'. Blue circles describe the oxygen atoms. (b) The tetragonal unit cell of SFMO. (c) Schematic picture of the SFMO structure. Inside the oxygen octahedra are Fe and Mo atoms, which alternate in the structure. The Sr atoms are positioned in the cubes formed by the octahedra.

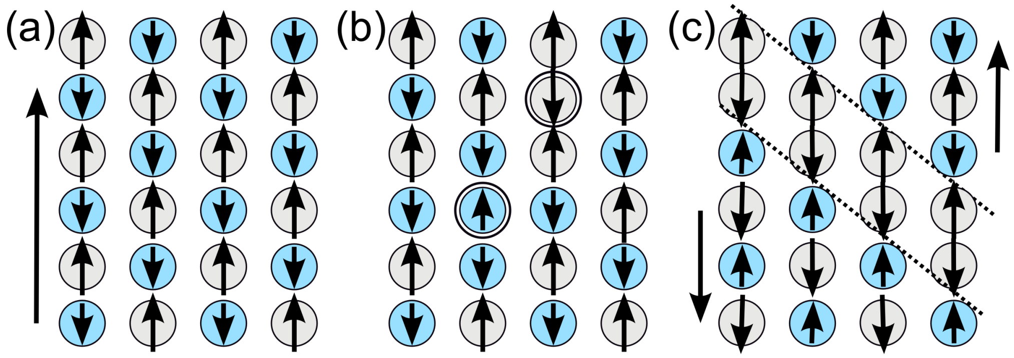

Figure 5. Schematic picture of the B-site structure of SFMO described with gray (Mo) and blue (Fe) circles. The small arrows represent the magnetic moments of the atoms and the larger arrows represent the total magnetization. (a) The optimal ordering of the SFMO without ASD. (b) The antisite disorder as a point defects, where one Mo atom is replaced with Fe atom and vice versa. (c) The antiphase boundary formed by the misplaced Fe atoms. The both sides of the boundary as well as the boundary itself are antiferromagnetically ordered, but the total magnetic moments on each side can be in opposite directions.

According to the band structure calculations, SFMO is a half metallic ferrimagnet, which has a gap at the Fermi level in the majority spin channel and 100 % spin polarized charge carriers [17, 41, 42]. The ferrimagnetic ordering in SFMO results from the antiferromagnetic coupling between the magnetic Fe^{3+} and Mo^{5+} ions, which leads to the saturation magnetization, M_s, of 4 μ_B/f.u.. However, it has been shown that the valence of Fe can also be 2+ instead of 3+ and similarly the valence of Mo can be 6+ instead of 5+ [43, 44]. The $Fe^{2+}Mo^{6+}$ configuration leads to a ferrimagnetic ground state with exactly same saturation magnetization than the common $Fe^{3+}Mo^{5+}$ configuration. The valence mixing enables also the double exchange type interaction in Fe^{3+}-O-Mo-O-Fe^{2+}, which involves itinerant electrons [45]. As a consequence of the itinerant electrons, the net moment reduces from 4 μ_B/f.u. to 3.5 μ_B/f.u. [45]. A schematic description of the superexchange type interaction in the $Fe^{3+}Mo^{5+}$ and $Fe^{2+}Mo^{6+}$ configurations assuming cubic symmetry is presented in figure 6(a) and (b), respectively. In reality, the slight tetragonal distortion changes the typical t_{2g} and e_g splitting into a more complicated configuration of three singlet states and doublet state [46].

The ferro-paramagnetic transition temperature of SFMO is exceptionally high among half metals. According to the theoretical calculations, the Curie temperature, T_C, is around 450 K [17, 32]. Experimental values for T_C show large variation depending on the sample type and quality. In polycrystalline and single crystal samples, values around 420 K have been reported [17, 47–49], but the T_Cs of thin films have not reached as high values. The published Curie temperatures for SFMO films have mostly been around 350 K, which are clearly lower than in bulk samples [23, 28, 50]. However, the determination and interpretation of the T_C is not explicit and values over 400 K have also been reported for the SFMO thin films [23, 51]. An example of a typical temperature dependence of magnetization for polycrystalline SFMO is shown in figure 7.

The resistivity properties and mechanisms of SFMO are highly dependent on the sample type, but a large negative magnetoresistance *i.e.* large decrease of resistance in applied magnetic field is observed as an intrinsic property. In polycrystalline samples, the MR is dominated by the tunneling of spin polarized charge carriers through grain boundaries [52–55]. The electron hopping between the grains is enhanced by the alignment of the magnetization of the grains due to the applied field, which causes the decrease in resistivity [17]. The low field response of the intergrain tunneling magnetoresistance is highly dependent on the grain size, oxygen content at the grain boundaries and the formation of the antiphase boundaries [56–58]. The high field response is more affected by the ASD and the low field MR is insignificant in highly disordered

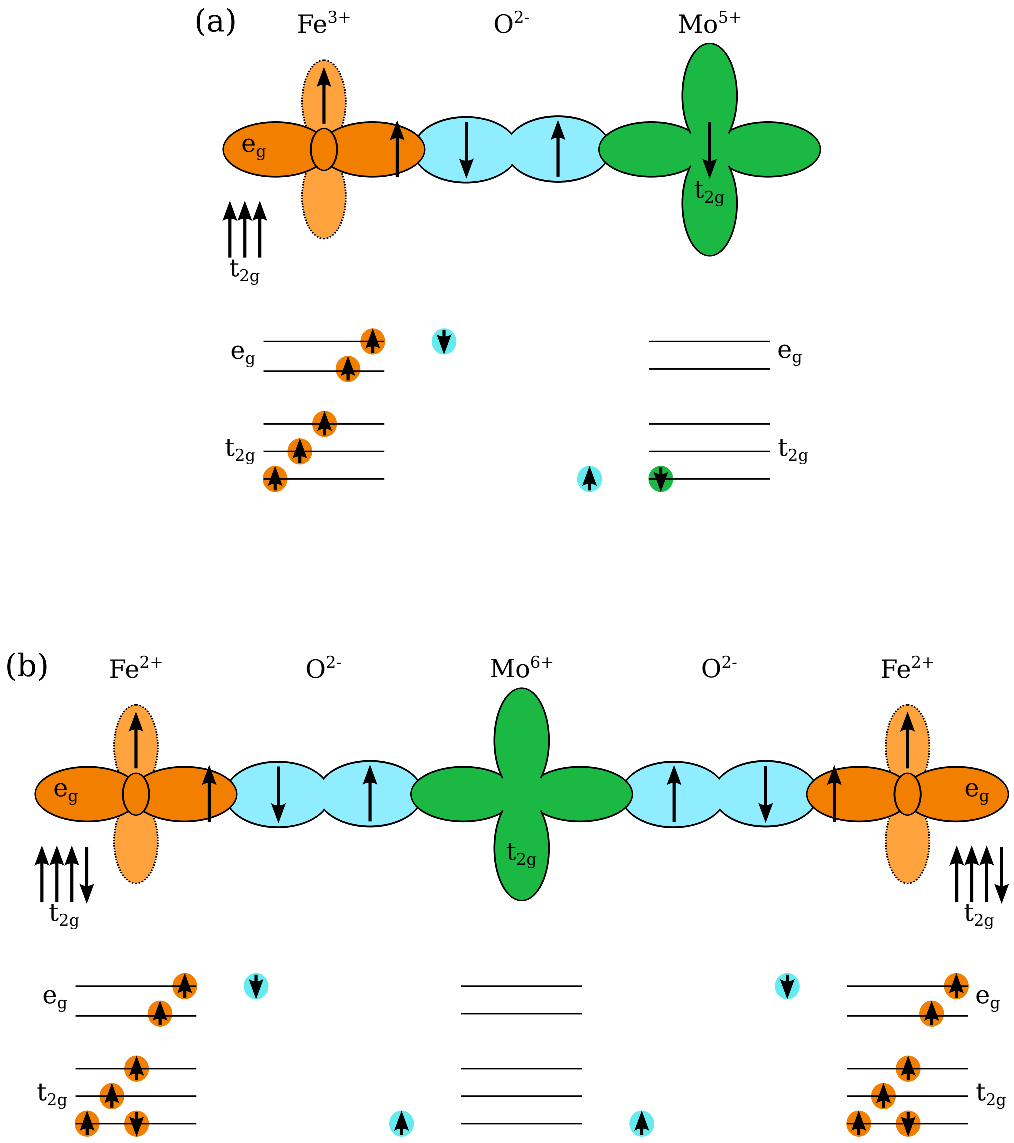

Figure 6. Schematic figure of the superexchange type interactions in the possible (a) $Fe^{3+}Mo^{5+}$ and (b) $Fe^{2+}Mo^{6+}$ configurations of SFMO.

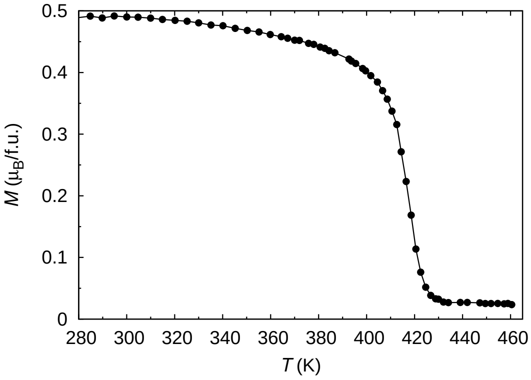

Figure 7. Temperature dependence of magnetization measured in 8 mT field for SFMO powder sample. The used data is from the publication of Suominen *et al.* [48].

samples [59, 60]. This suggests that the low field MR in SFMO is more dependent on the half metallicity and the spin-dependent intergrain scattering, whereas the high field MR is more an intragrain property and arises from the spin alignment under magnetic field [60]. The negative MR is also observed in single crystals and epitaxial thin films, but it is one order of magnitude smaller than in the polycrystalline samples [54]. The intergrain tunneling cannot explain the magnetoresistance in these type of samples and the mechanism of MR in single crystals and epitaxial thin films is still unclarified. The experimental results by D. Sánchez *et al.* and the theoretical studies by V. Singh *et al.* have suggested that the MR in thin films arises from the suppression of antiferromagnetically ordered ASD domains and is highly dependent on the amount of ASD [33, 36]. However, the role of possible low angle grain boundaries and dislocations in MR of SFMO thin films cannot be neglected.

The temperature dependence of resistivity of an ideal SFMO is metallic, which is not observed in real samples. In polycrystalline SFMO samples, the resistance is too high to be metallic and the temperature dependence shows semiconductive type behaviour [17, 54, 58]. This indicates that the resistance is dominated by the carrier scattering at the grain boundaries and the separate grains could be metallic [17]. In single crystals and epitaxial thin films, a metallic resistivity with a low temperature upturn in the temperature dependence has been reported [23, 29, 51, 54, 61, 62]. However, the physical origin of this complex resistivity behaviour has not been explained.

2 Experimental details

2.1 Sample preparation

The target has a significant role in the quality of the deposited film, because the material is stoichiometrically transferred from the target to the substrate. The SFMO targets can be made with a sol-gel-method [47, 63–68] or with a solid state reaction [23, 26, 27, 33, 50, 69–71]. In the sol-gel method, the solution of the starting ingredients is dried and rapidly fired before annealing. In the solid state reaction, the starting ingredients are powders, which are ground together before heat treatments. The solid state reaction requires high temperatures and long annealing time, which leads to a larger grain size of the resulting powder. In this work, the used target is made from the powder synthesized by sol-gel method as described in [47, 48]. The obtained powder was pressed to a pellet with 30 MPa pressure and sintered for 12 h at 1050 °C. The sintering atmosphere was flowing ArH_2(5 %) and the flow rate was 0.01 l/min. The grain size of the target was around 500 nm and the lattice parameters were $a = 5.587$ Å and $c = 7.970$ Å. The Curie temperature of the target was found to be around 400 K and the saturation magnetization at 10 K around 1.93 μ_B/f.u..

The SFMO thin films were fabricated with pulsed laser deposition (PLD), which is a well-suited method to grow high quality crystalline thin films of complex oxides. In addition to the cost-effectivity and simple growth technique, the advantages of the PLD are the stoichiometric transfer of material from the target to the substrate, epitaxial film growth and the success in depositing large variety of materials including multicomponent compounds. Therefore, the PLD is the most used preparation method for SFMO thin films, even though other methods like chemical solution deposition (CSD) [72–74], chemical vapor deposition (CVD) [75] and magnetron sputtering [62, 76, 77] have also been used. In the PLD process, the laser pulses hit a pure stoichiometric target, which is placed in a vacuum chamber. Due to an increased energy density, the laser pulses vaporize material from the surface of the target and form a plasma plume. The tip of the visible plume is adjusted to hit a heated substrate where the film is created. A schematic picture of the used deposition system is shown in figure 8. In PLD, single crystal substrates are often used to obtain epitaxially grown crystalline films. The substrate is generally chosen to have well matching crystal lattice with the film material. This minimizes the strain and defect formations, which arise when the in-plane lattice of the film material is compressed or elongated according to the substrate crystal structure. Typical substrates for perovskite films are for example $SrTiO_3$ and $(LaAlO_3)_{0.3}(Sr_2AlTaO_6)_{0.7}$,

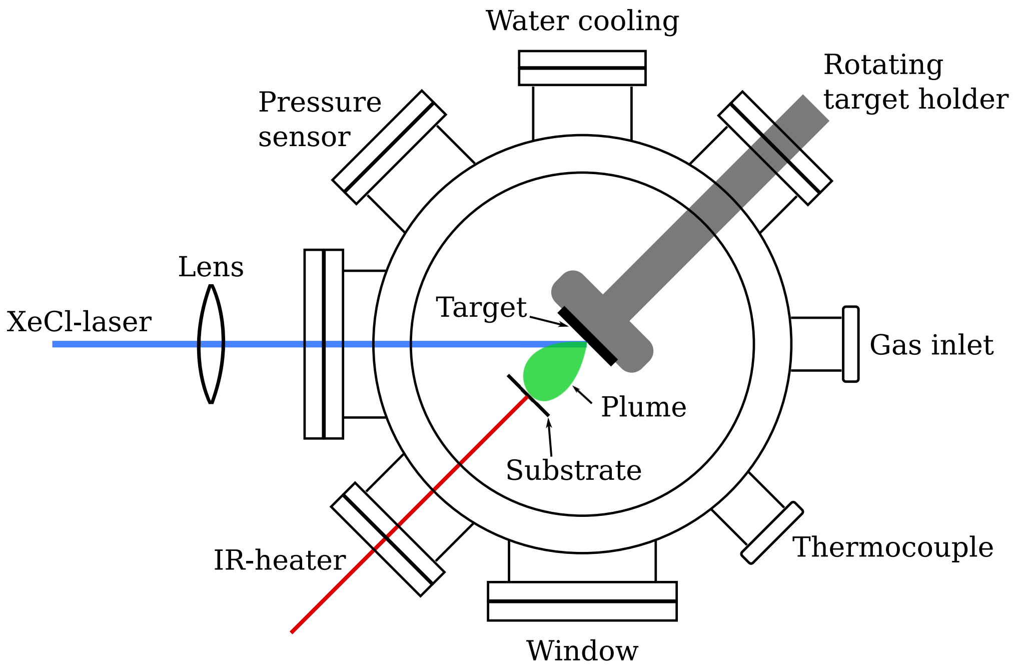

Figure 8. Schematic picture of the pulsed laser deposition chamber and the main components of the setup.

because of the well matching crystal lattice with various perovskite materials. The substrate materials used in this work and their effect on the properties of SFMO films are discussed in more detail in section 5.

The growth of SFMO with pulsed laser deposition requires fairly high substrate temperatures and specific atmosphere. The optimization of the deposition parameters for SFMO is described in detail in section 3, but the typical deposition procedure is the following. The substrate is heated to a desired temperature at 25 °C/min and the deposition atmosphere of Ar or ArH_2(5%) is adjusted to the deposition pressure. The ablation is done using the XeCl excimer laser ($\lambda = 308\,\text{nm}$) with the laser fluence of $2.5\,\text{J/cm}^2$ and the pulse frequency of 5 Hz. After deposition, the film is annealed in the deposition atmosphere and temperature for 10 min and cooled down to the room temperature at 25 °C/min. The pulse number was varied from 500 to 8000 pulses to obtain different film thicknesses. Unless otherwise noted, the pulse number of 2000 has been used, which results in around 150 nm thick films.

2.2 Structural characterization

The X-ray diffraction (XRD) was used in the structural investigations of the SFMO thin films as well as to verify the good quality of the target. In XRD, the X-rays are diffracted from the lattice sites of the investigated material. Due to the periodicity of the lattice, a constructive interference according to Bragg's law is formed for the specific lattice planes in a certain diffraction angle [78]. In this work, the XRD measurements were carried out with the *Philips X'pert Pro MPD* diffractometer in the Bragg-Brentano θ-2θ configuration. The Cu K_α radiation, Ni filter and a Schulz texture goniometer were used in all the measurements.

The phase purity of the films and the target was ensured with the general $\theta - 2\theta$ scans. The texture measurements of the SFMO (204) peak ($2\theta = 57.106^\circ$) were carried out to determine the orientation and texturing of the thin films. The texturing of the typical impurity phase peaks of $SrMoO_4$ (112) at $2\theta = 27.68^\circ$ and Fe (110) at $2\theta = 44.98^\circ$ were measured in certain cases to confirm the phase purity of the films. The SFMO (204) peak has also been measured in more detail with the 2θ-ϕ scans and it has been used in the determination of the lattice parameters, strain and the full width at half maxima (FWHM). The detailed $\theta - 2\theta$ scans of the (206), (336) and (404) peaks were measured to determine the lattice parameters with the Nelson-Riley method, which minimizes the systematical errors [79]. In more detailed structural analysis of the films, the microstrain in c direction was determined with the Williamson-Hall method [80]. The reflectivity measurements, made with the incident beam X-ray mirror, were used to determine the film thicknesses from the films made with less than 2000 pulses.

The reciprocal space maps of all the eight (101) and (404) peaks were used in the determination of the ASD. The (101) of SFMO is a superstructure line meaning that its intensity increases by improved B-site ordering [35, 81], while the intensity of the (404) peak is independent on the Fe/Mo-ordering. The effect of ASD on the (101)/(404) intensity ratio was simulated with the Fullprof Rietveld refinement program [82, 83] and the simulated intensity ratio dependence of the B-site ordering is shown in the inset of figure 9(a). The integrated intensities were determined by fitting a Lorentzian peak into the ω-projection of the peaks, which includes the data of whole 2θ range (see figure 9(b)). This enables to separate the SFMO peaks from the substrate peaks, which is problematic especially in the films on STO. The B-site ordering was determined with a function $B_{\mathrm{ord}} = \sqrt{I(101)/I(404)/a} + b$, where I is the integrated intensity of the peak and $a = 0.5583 \pm 0.0005$ and $b = 0.4775 \pm 0.0002$ are constants obtained from the simulation of the XRD intensities. The peaks for the intensity ratios were chosen to be

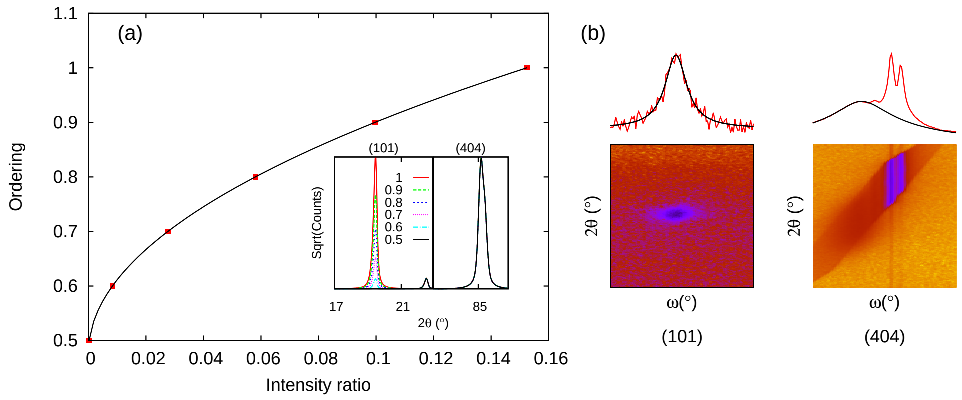

Figure 9. (a) The curve used to determine the ASD from the intensity ratio of (101)/(404) peaks. The inset shows the simulated peak intensities with different disorder levels. (b) Reciprocal space maps of (101) and (404) peaks of the example film on STO in logarithmic scale. The large peaks and the background features in the (404) image arise from the substrate. Above the images are shown the ω-projections from where the intensities were determined. [**P5**]

at the same tilt angle ψ so that one does not have to determine geometric corrections related to ψ in the Schulz goniometer. The geometric corrections due to different θ are taken into account in the simulation.

The oxygen vacancy concentrations of the films were investigated with the hard X-ray photoelectron spectroscopy (HAXPES) using the valence spectra together with the calculated density of states and spectra of the Mo 3d, Sr 3d and O 1s core levels. The spectra were obtained at the BESSY II in the Helmholz-Zentrum Berlin using the HIKE end-station of the KMC-1 beamline [84]. The measurements were carried out at room temperature using photon energy of 5000 eV and grazing incidence geometry with normal emission. The calibration of the binding energy scale was done with the Au $4f_{7/2}$ core levels of the calibration sample.

Atomic force microscopy (AFM) was used to characterize the surface structure and roughness of the films. The AFM investigations were made with the *Park Scientific Instruments AutoProbe research system* in a contact mode. The AFM imaging is based on the scanning of the film surface with a nanometer scale tip, which is positioned at the end of a cantilever. Due to the repulsive van der Waals forces between the sample and the tip in the contact mode, the cantilever is deviated from the surface according to the surface structure. The movement of the cantilever is detected with a laser beam reflected from the cantilever and the scanning is caused by moving the sample with a piezoelement. The root mean square roughness of the films were determined as an average of the several AFM images taken with different image sizes from $2 \times 2\,\mu\mathrm{m}^2$ to $20 \times 20\,\mu\mathrm{m}^2$. The thicknesses of certain films were also determined with AFM over an edge chemically etched with nitric acid.

The microstructure of the films was determined with the transmission electron microscopy (TEM) in Max Planck Institute of Microstructure Physics (Halle, Germany). The samples were prepared for cross-sectional imaging by fabricating focused ion beam (FIB) lamellas. High resolution TEM (HRTEM) imaging was performed with a JEOL JEM-4010 electron microscope at an accelerating voltage of 400 kV. Also, a probe-corrected scanning TEM using high-angle annular dark field imaging (HAADF STEM) were performed with TITAN 80-300 at the voltage of 300 kV. The TEM images were used to determine the substrate/film interface effects, defect formation and the film thickness.

2.3 Magnetic and magneto-transport measurements

Magnetic measurements of the thin films and the target were made with SQUID magnetometers. These magnetometers work with the induction method, where the magnetic moment is detected by moving the sample inside pick-up coils. The pick-up coils are inductively connected to a RF SQUID loop. The applied magnetic flux through the SQUID induces supercurrent around the loop, which causes a modulation of the current in the inductively coupled LC resonant circuit. The applied magnetic field used in the measurements is created with superconducting magnets. In this work the *Cryogenic Limited S600X* and the *Quantum Design MPMS XL* SQUID magnetometers were used. For the Cryogenic's magnetometer, the samples were attached to copper wire with a Teflon tape and for Quantum Design's magnetometer, the samples were attached to plastic straw with a Kapton tape.

The temperature dependence of the magnetization was typically measured in 100 mT field, but also 500 mT applied field was used. The Curie temperatures were determined from the magnetization curves either as the point where the magnetization deviates from the minimum (onset T_{C}) or as the minimum of the temperature derivative. The magnetic hysteresis loops were measured at several different temperatures, typically at least at 10 K, 300 K and 400 K. The hysteresis loops were used to determine the coercivity field and the saturation magnetization. In all magnetic measurements the applied magnetic field has been parallel to the plane of the film, *i.e.* along the SFMO (001) plane.

The magneto-transport properties of the films were measured with the *Quantum Design PPMS* magnetometer using the resistivity option. The resistance was measured as a voltage through the film with constant 100 μA current using two thin copper wires connected to the surface of the film with In. The four-point measurement was not considered necessary due to the high resistance of the samples. The external magnetic field up to 8 T was created with superconducting magnets. The temperature dependence of resistivity was measured in zero field and with several magnetic fields from 50 mT to 5 T. The magnetoresistance was measured from −8 T to 8 T at different temperatures from 10 K to 350 K. In all magneto-transport measurements the applied magnetic field was perpendicular to the plane of the film.

3 Optimization of the thin film fabrication process

3.1 Deposition temperature and atmosphere

The deposition parameters have a significant role in the quality of pulsed laser deposited SFMO thin films, especially in the formation of impurity phases and defects. Earlier investigations have shown that the formation of impurity phases and ASD is enhanced at low deposition temperatures, T_{d}, and the properties of SFMO thin films can be improved by increasing the T_{d} at least up to 1000 °C [25, 27, 29, 61, 85, 86]. In addition to the T_{d}, oxygen atmosphere with pressure higher than 0.01 Pa has been seen to promote the formation of impurities like $SrMoO_4$ [50, 69]. However, impurity free SFMO thin films have been fabricated in higher pressures using inert Ar atmosphere, reductive ArH_2 atmosphere, vacuum conditions or atmospheres where small amount oxygen is mixed with Ar or N_2 [23, 27–30, 33, 70, 71, 85–88].

In order to find the optimal deposition temperature and atmosphere, two series of SFMO films were made on $SrTiO_3$ substrate. The first series was made with varying the T_{d} from 800 °C to 1150 °C with 50 °C intervals. The other series was made at the optimized deposition temperature with different pressures of ArH_2(5 %) and also one in Ar atmosphere. The used deposition atmospheres together with the main structural and magnetic properties of the films are presented in table 1. According to the XRD measurements, all the films in both series were phase pure, epitaxially textured and c-axis oriented. The lattice parameters did not show systematical variation with the deposition temperature or atmosphere, but the c parameter was shorter and the $a = b$ parameter was longer than observed for the target. Together with the FWHM in 2θ and ϕ determined from the (204) peak, these imply that the films are under fair amount of stress. Also, the H_2 content of the deposition atmosphere induces a clear increase in 2θ-FWHM and c parameter (films 4, 5 and 6).

Even though the lattice parameters and FWHM did not show reasonable deposition temperature tendency, the growth mode of the SFMO films changes with T_{d}, as seen from the AFM images in figure 10. The almost 2D-growth at lower temperatures changes to island growth when the deposition temperature is around 950 °C. At low T_{d}, the film surface has small droplets on a relatively smooth surface, but the island size and the background roughness increase and also small holes are formed with increasing T_{d}. Also, the surface particle size and the RMS roughness increase with the deposition temperature up to 1100 °C. The deposition atmosphere, however, does not affect the RMS roughnesses of the films, apart from the film 3 grown in higher pressure, where

Table 1. The key properties of the films deposited at 1050 °C in different atmospheres. The magnetization at 300 K is listed as percents of the 5 K value. [**P1**]

Film	Atmosphere	T_C (K)	M 5 K μ_B/f.u.	M 300 K %	a/b (Å)	c (Å)	2θ FWHM (°)	ϕ FWHM (°)	RMS roughness (nm)
1	0.07 Torr Ar/5 % H_2 flow	375	1.22	15	5.59	7.89	0.32	0.97	1.28
2	0.04 Torr Ar/5 % H_2 no flow	344	1.22	12	5.64	7.89	0.34	0.98	3.32
3	0.1 Torr Ar/5 % H_2 flow	336	0.90	36	5.60	7.88	0.38	1.07	6.39
4	0.02 Torr Ar/5 % H_2 flow	< 300	0.58	4	5.63	7.93	0.59	1.13	2.39
5	< 0.005 Torr Ar/5 % H_2 no flow	< 300	0.57	15	5.62	7.94	0.46	1.04	2.78
6	0.07 Torr Ar flow	341	0.925	16	5.61	7.90	0.62	1.05	2.98

the roughness is clearly larger when compared to others.

The Curie temperature together with the saturation magnetization and the spin polarization are the most important parameters in the optimization of the SFMO thin films for the possible applications. The zero field cooled (ZFC) and field cooled (FC) magnetization curves of the film grown at 1050 °C measured in 100 mT field are shown as an example in figure 11. In many of the samples, the magnetization curves revealed a small paramagnetic signal, even above T_C. This is most likely due to a ferromagnetic impurity like metallic Fe clusters in amount less than the XRD detection limit of 1 %. The magnetic signal from 1 % of Fe in the SFMO sample is the same order of magnitude as observed in the films.

The onset Curie temperatures of the films were determined from the $M(T)$-curves as the point where the curve deviates from the constant paramagnetic part. The deposition temperature dependence of the onset Curie temperature is presented in figure 12(a). It shows that the highest T_C, close to 340 K, is observed with T_d from 950 °C to 1050 °C. The saturation magnetization could not be reliably determined from the hysteresis loops, because the signal of the ferromagnetic impurity cannot be subtracted. Instead, the magnetization difference, M(100 mT), between 5 K and 400 K magnetization values was determined from the $M(T)$-curves. It was used to estimate the changes in saturation magnetization even though the films are not at full saturation in 100 mT.

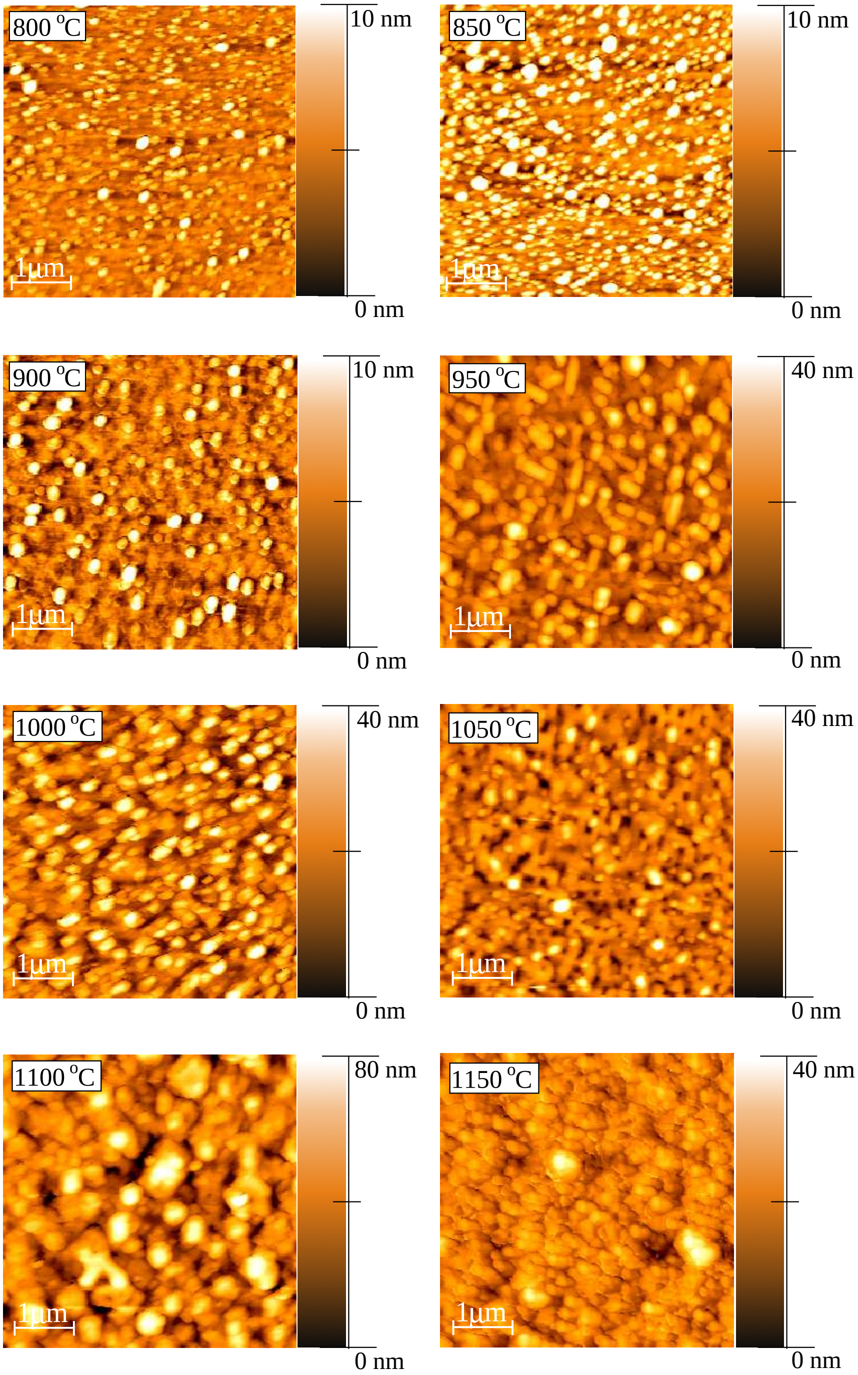

Figure 10. The $5 \times 5\,\mu\mathrm{m}^2$ AFM images of the films grown with different deposition temperatures showing the changes in the surface morphology. The deposition temperatures are marked on the image. [**P1**]

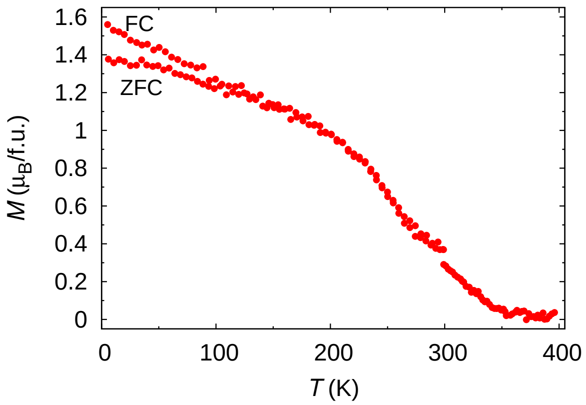

Figure 11. Temperature dependence of magnetization measured in 100 mT field for the film grown at 1050 °C. [**P1**]

The deposition temperature dependence of M(100 mT) is shown in figure 12(b). The M(100 mT) and also the saturation magnetization inevitably increases with increasing deposition temperature. The changes in saturation magnetization has been earlier related to the B-site ordering and the observed increase is most likely a result of the lower ASD concentration [26, 32, 70].

The magnetic properties listed in table 1 show a strong dependence of the deposition atmosphere. The highest Curie temperature and low temperature magnetization is observed in film 1, which is grown with 9 Pa pressure Ar/H_2(5 %). The T_C is clearly reduced with lower and higher deposition pressures, but the decrease is larger when low pressures are used. The sharpest ferro-paramagnetic transition and highest magnetization at 300 K in relation to the 5 K value is obtained with 13 Pa pressure (film 3). However, the T_C and the 5 K magnetization are not as high as in film 1 and the RMS roughness is notably larger than in other films.

Based on these results, the optimal deposition temperature for pulsed laser deposited SFMO thin films is 1050 °C. Even though the film grown at 1050 °C, does not have the optimal surface smoothness, it has the highest Curie temperature and relatively high saturation magnetization among these films. This suggest fairly good B-site ordering in film grown at 1050 °C. Also, no indication of the ferromagnetic impurity seen in many other samples was observed in the magnetization curve. The optimal deposition atmosphere for SFMO films is clearly 9 Pa pressure Ar/H_2(5 %), because it results in highest T_C and M(5 K). It also leads the best structural properties including smallest

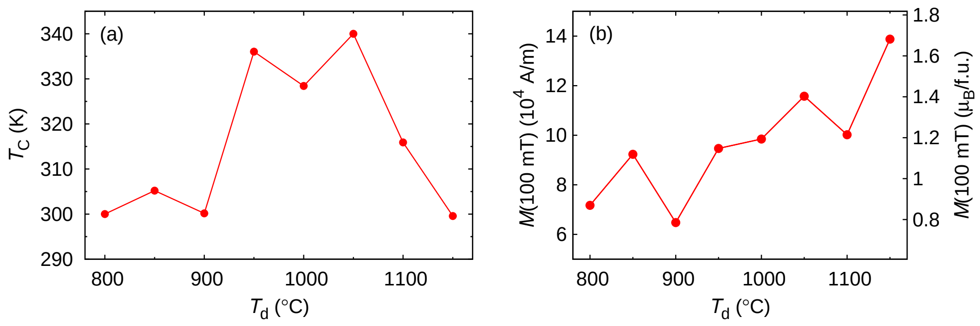

Figure 12. (a) The deposition temperature dependence of the T_C. (b) The magnetization difference between 5 K and 400 K in 100 mT field. The values are shown in units of A/m on the left hand scale and on the right hand scale in units of μ_B/f.u.. [**P1**]

surface roughness and the lattice parameters are closest with the used target. However, after the used PLD system was upgraded, the deposition atmosphere was re-optimized as the optimal atmosphere is among other things dependent on the pumping capacity etc. It was found that the 9 Pa pressure Ar atmosphere should be used instead of the earlier Ar/H_2(5 %) atmosphere. Hence, the Ar/H_2(5 %) was used in [**P1**-**P4**], but Ar atmosphere were used in [**P5**] and [**P6**].

3.2 *Ex situ* post-annealing treatments

The magnetic properties of SFMO thin films are not as good as in polycrystalline samples or in the target used in their deposition despite the optimization of the deposition parameters. Previous experiments with the polycrystalline SFMO samples have shown that the B-site ordering could be improved by increasing the sintering temperature [34]. In SFMO thin films, a better cationic ordering is earlier achieved by reducing the growth rate, which gives material more time to settle [33]. The properties of the SFMO films have also been improved by oxygen treatments after deposition [35, 89]. The post-annealing treatments have been shown to induce significant changes in the structural and magnetic properties of manganite films, which have similar magnetic and half metallic properties with SFMO [90–93]. Therefore, the effect of different *ex situ* post-annealing treatments on SFMO films was investigated.

The *ex situ* post-annealing treatments were carried out to four as-deposited SFMO films, which were cut into 4 pieces each before the treatments. The high quality of

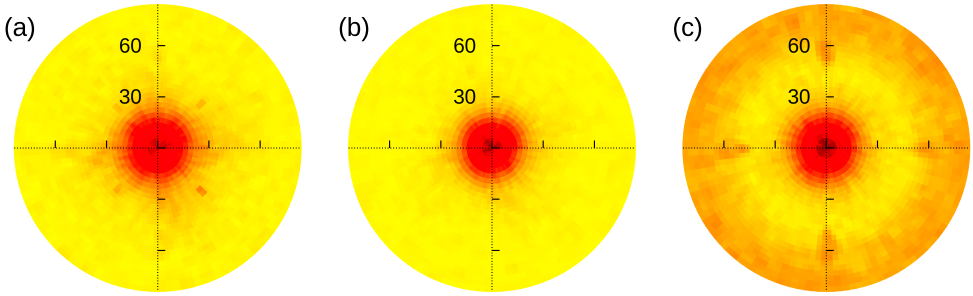

Figure 13. The pole figures of the (a) SFMO (204), (b) Fe (110) and (c) $SrMoO_4$ (112) peaks in the logarithmic scale for the sample Ar annealed at 900 °C. [**P2**]

the as-deposited films was confirmed with XRD measurements. Ar, Ar/H_2(5 %) and air atmospheres together with the vacuum annealing in 1×10^{-2} Pa were used in the treatments. The post-annealing time was 10 h and the used temperatures were 500 °C, 700 °C, 900 °C and 1100 °C. As a result of the annealing treatments in air, the SFMO films had a bright yellow colour indicating the dominance of the $SrMoO_4$ impurity phase. Also, the Ar annealed samples contain some $SrMoO_4$ as can be seen from the pole figures presented in figure 13. The one for SFMO (204) in figure 13(a) does not show clear peaks, instead $SrMoO_4$ peaks are clearly visible in figure 13(c). In vacuum and Ar/H_2(5 %) treated samples, no indication of impurity phases were observed in the $\theta - 2\theta$ scans or in the texture measurements. The Ar/H_2(5 %) treatment did not change the length of the c parameter, but the a/b parameter was decreased. The vacuum annealing increased all lattice parameters. This could be related to the removal of oxygen, which increases the length of a/b parameter [**P6**]. The RMS roughness was not affected by the Ar/H_2(5 %) and vacuum treatments, but it was increased with increasing annealing temperature in Ar annealed samples.

The magnetic properties were not improved nor worsened with Ar/H_2(5 %) and vacuum anneals. The ZFC and FC magnetization curves in figure 14 show that the T_C and the shape of the ferro-paramagnetic transition have not changed with Ar/H_2(5 %) and vacuum treatments. However, these samples have similar paramagnetic signal above Curie temperature, that was observed in the optimization of the deposition temperature and atmosphere [**P1**]. The paramagnetic signal does not change from the as-deposited sample with Ar/H_2(5 %) treatments, but it clearly increases with vacuum annealing. As mentioned before and in the following sections, the paramagnetic signal originates most likely from the Fe or Fe-oxide clusters. The magnetization of the Ar annealed sample is

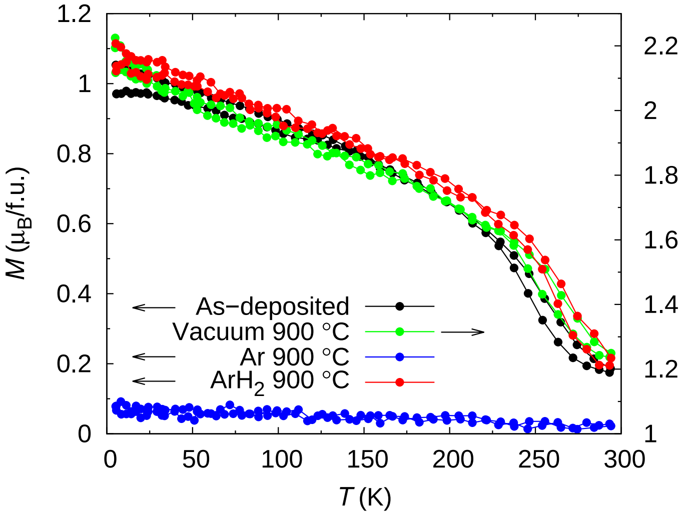

Figure 14. Temperature dependence of magnetization measured in 100 mT for as-deposited films and films post-annealed at 900 °C in different atmospheres. The magnetization values of vacuum annealed sample are given on the right hand scale. [**P2**]

basically constant in the whole temperature range and this confirms the XRD observations of the nonmagnetic $SrMoO_4$ impurity phase. Altogether, the *ex situ* post-annealing treatments did not show significant modification of the structural and magnetic properties compared to the as-deposited film aside from the formation of the impurity phases. This means that the properties of SFMO thin films could not be improved by this type of annealing treatments. However, later *ex situ* post annealing treatments in ultra-high vacuum conditions has been seen to induce oxygen vacancies and change the magnetic properties of SFMO film as will be discussed in the section 6.

4 The influence of strain and film thickness

Thin films are always under some strain due to the lattice mismatch between the film and used substrate. Therefore, the choice of a substrate has an important role in the quality of the film. In case of SFMO thin films, the choice of substrate is discussed more detail in the section 5. Because the strain is induced from the substrate to the film, the film is more strained near the interface and the lattice parameters of the film relax towards the bulk values when the film thickness is increased [33, 76, 94]. Hence, the strain of the film can be varied by changing the film thickness, even though the relaxation is not necessarily linear. For example, the lattice parameters of SFMO films on STO with different thicknesses have suggested that the films are fully strained below critical thickness of 34 nm and fully relaxed with thicknesses above 80 nm [94]. However, the relaxation is strongly affected by the lattice mismatch between the film and the substrate [95].

The film thickness and thereby the strain has been seen to affect both the structural and magnetic properties of the SFMO thin films. In most cases, the surface roughness increases and the surface morphology changes with increasing thickness [76, 95, 96]. The microstructure is also different for films with different thicknesses and films are seen to relax through stacking faults, when the thickness is increased [94, 97]. In manganite thin films, which have many similar properties with SFMO, the magnetic and resistivity properties are strongly related to the lattice mismatch induced strain and film thickness [98, 99]. In SFMO thin films, the results of film thickness dependent magnetic properties are not consistent. The saturation magnetization has been seen to both increase and decrease with increasing thickness, depending on the used substrate and fabrication method [33, 62, 97]. However, using different substrates with different lattice mismatches most likely induce some other interface defects in addition to the strain, which could also affect the magnetic properties of the films.

In this work, two series of SFMO films with different thicknesses were grown on single crystal $SrTiO_3$ substrate to investigate the effect of film thickness and strain. In the first series (thicker-film series), the film thickness was increased from the value used in the optimization of the deposition parameters and the films were made in $Ar/H_2(5\,\%)$ atmosphere. In the second series (thinner-film series), the film thickness was decreased from the value used in the optimization of the deposition parameters and the films were made in Ar atmosphere. Pulse numbers of 2000 (S2), 4000 (S4) and 8000 (S8) were used in the thicker-film series and 500 (S500), 1000 (S1000), 1500 (S1500) and 2000 (S2000) in the thinner-film series. The thicknesses of the films in the thicker-film se-

Table 2. The film thicknesses and the lattice parameters of the samples grown with different pulse numbers. [**P4**, **P6**, SI]

Film	Pulse number	Thickness (nm)	a (Å)	c (Å)
S500	500	49^*	5.531	7.952
S1000	1000	81^*	5.539	7.951
S1500	1500	123^*	5.558	7.936
S2000	2000	160^*	5.558	7.931
S2	2000	$150^\dagger$	5.532	7.952
S4	4000	$270^\dagger$	5.610	7.928
S8	8000	$500^\dagger$	5.595	7.904

*Determined with XRD reflectivity measurement.
†Determined with AFM profilometry.

ries were determined with AFM profilometry and in the thinner-film series, XRD reflectivity measurement together with the TEM images were used to determine the film thicknesses. All the thicknesses with the used pulse numbers are shown in table 2.

4.1 Structural properties

The XRD measurements confirmed the phase purity and epitaxial texturing of the films with the exception of the thickest S8 sample. The θ-2θ scans of the films in figure 15(a) and (b) show the (00l) peaks of the substrate and the film. A small impurity phase peak near 50° is observed only for S8 and similar peak was also seen near 25°, which suggest the presence of Fe_2O_3 in S8 sample. The pole figures of the texture scans showed only sharp (204) and (132) peaks for all the samples.

The lattice parameters of the films in the thicker-film series were determined from the (00l) peaks in the θ-2θ-scans and from the θ-ϕ-scans of (204) peak using STO as internal standard. For the thinner-film series, the c parameter was determined from the (00l) peaks of θ-2θ-scans using the Nelson-Riley method and the a parameter from the detailed θ-2θ-scans of (336) peak. The lattice parameters of the both series are presented in table 2. Because of the differences in determination, the lattice parameter values of these series cannot be directly compared. The films in these series were also made in different atmospheres, which could affect the absolute lattice parameter values for example through oxygen vacancies. In the thicker-film series, the a parameter in-

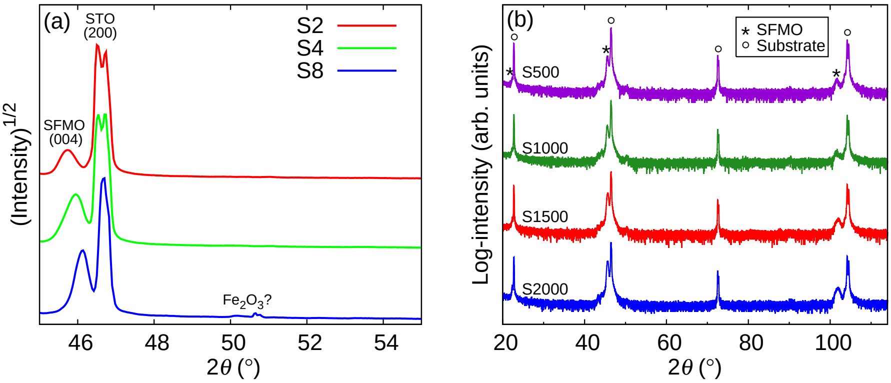

Figure 15. (a) Detail of the θ-2θ scans for the films in thicker-film series. (b) The overall θ-2θ scans of the films in thinner-film series. The SFMO (00l) peaks are indicated with asterisks and the substrate (00l) peaks with open circles. [**P4**, **P6**, SI]

creases with increasing thickness from 150 nm to 270 nm, but is approximately same in the 270 nm and 500 nm thick films. The lattice parameter a increases with increasing thickness also in the thinner-film series, but is already equal in the 123 nm and 160 nm thick films.

The lattice parameters of the films in the thinner-film series were also used to determine the in-plane, ε_a, and out-of-plane, ε_c, strains with the equations

$$\varepsilon_a = \frac{a - a_\mathrm{b}}{a_\mathrm{b}} \quad \text{and} \quad \varepsilon_c = \frac{c - c_\mathrm{b}}{c_\mathrm{b}}, \tag{7}$$

where the $a_\mathrm{b} = 5.575$ Å and $c_\mathrm{b} = 7.893$ Å are the lattice parameters of the bulk SFMO [100]. A negative in-plane strain and positive out-of-plane strain were observed in all the films of the thinner-film series, which means that when the a parameter decreases the c parameter increases from the bulk values *i.e.* the Poisson coefficient is positive. Also, both the ε_a and ε_c were seen to decrease with increasing thickness up to 123 nm suggesting that the films are relaxed at thickness between 80 nm and 120 nm. Earlier investigations have also shown the lattice relaxation at around 80 nm in SFMO thin films on STO [94]. The comparison of the bulk values and the lattice parameters of the films in the thicker-film series show that the 150 nm S2 sample is more strained than the thicker films, which indicates that the relaxation occurs also at larger thicknesses. However, in the S4 and S8 samples, both a and c parameters increase from the bulk values, which is not the case in any other samples, and indicate that they might have larger amount of structural defects.

The FWHM values in 2θ and ϕ, determined from the SFMO (204) peak, increased slightly with increasing thickness in the thicker-film series. The change in 2θ-FWHM was from 0.50° of the S2 sample to 0.75° of the S8 sample and correspondingly the ϕ-FWHM changed from 0.64° to 0.72°. Thus, the distribution of the unit cell volume through the film and the amount of low angle grain boundaries are increased as the thickness increases from 160 nm to 500 nm. However, the ϕ-FWHM in the whole thinner-film series was almost the same as in S2 sample without any thickness dependence aside from the slightly smaller value for S1000 sample. The FWHM of the $(00l)$ peaks in the thinner-film series was used to determine the microstrain, $\varepsilon_{\mathrm{WH}}$, which in this case describes the variation of the c parameter throughout the whole film thickness. However, no thickness dependence were observed in the $\varepsilon_{\mathrm{WH}}$ either. These suggest that more low angle grain boundaries and possibly other structural defects are formed when the film thickness is higher than 160 nm, which could also be related to the different deposition atmosphere. It seems that the variation in structural properties, despite the changes in strain, are small enough that they can be neglected at least when the film thickness is not more than 160 nm.

4.2 Magnetic properties

Magnetic measurements for these two series were made with different SQUID magnetometers (section 2.3) and the Curie temperatures were determined differently. In the thicker-film series, the measurements were made with the device from *Cryogenic* and the onset T_{C} was determined from the 100 mT $M(T)$-curve as described in section 3.1. The measurements on the thinner-film series were made with the *Quantum Design* magnetometer and the T_{C} was determined as a minimum of the 500 mT $\mathrm{d}M/\mathrm{d}T$-curve. Since, the uncertainty in these two T_{C} determination methods is similar, the comparison only within the series is reliable. Therefore, the absolute values for magnetic properties between the series should not be directly compared, but used to give an insight to their thickness dependencies.

The FC magnetization curves of the films in thicker-film series are shown in figure 16(a) and the onset T_{C} is pointed out with an arrow. Only small changes in T_{C} were observed and it slightly decreases with increasing thickness, which might be due to the higher amount of defects and the impurity phase observed in the thicker films. Figure 16(a) also show small deviation in magnetization at low temperatures between the films, but the changes can be neglected when the uncertainties in thickness determination are taken into account. Thus, it can be concluded that the magnetic properties

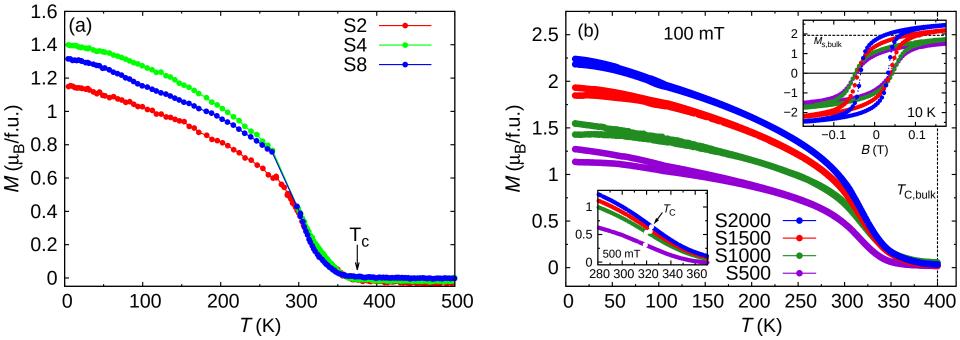

Figure 16. The temperature dependence of magnetization in 100 mT field for the films in (a) thicker-film series and (b) thinner-film series. The right inset of the (b) shows the magnetic hysteresis loops and the left inset shows the close-up of the ferro-paramagnetic transition for the films in thinner-film series. [**P4**, **P6**, SI]

of SFMO films do not significantly change with film thickness after threshold thickness around 160 nm is reached.

The temperature dependence of magnetization measured in 100 mT for the films in the thinner-film series is shown in figure 16(b). The ZFC and FC curves reveal small irreversibility and the temperature, where the curves deviate, increases with decreasing thickness and increasing strain. The magnetic field dependence of magnetization, presented at the top right inset of figure 16(b), shows that also the field required for saturation increases with decreasing thickness and the 100 mT field is not high enough for saturation. The increasing strain also causes slight skeweness to the hysteresis loops. The strain contributes to the total free energy that is minimized by the formation of the domain structure [1, p.234]. This way the strain can change the magnetic field response of SFMO and cause these changes between the films. It is commonly known that the structural defects cause the domain wall pinning and affect the domain motion and rotation. Even though the structural results showed that the amount of these kind of defects does not change within the thinner-film series, it is possible that they dominate closer to the interface and their effect on the magnetic properties, that are averages of the whole film, is reduced when the thickness is increased.

The Curie temperatures of the films in the thinner-film series are pointed out with white dots at the bottom left inset of figure 16(b). The changes between the films are quite small, only a slight increase with increasing thickness is observed. The saturation magnetization at 10 K shows similar, slightly increasing, tendency as the T_C. The

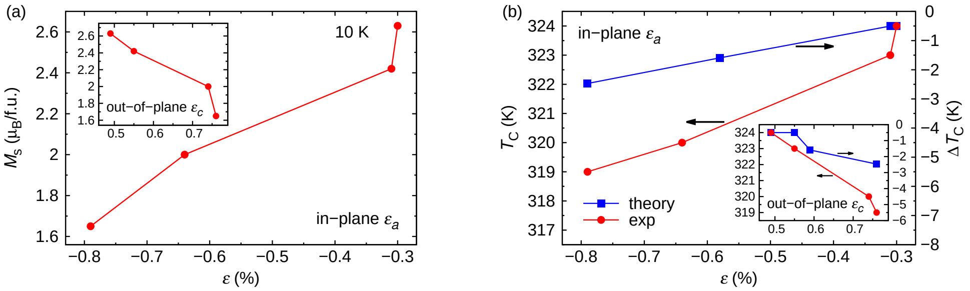

Figure 17. The saturation magnetization (a) and the Curie temperature (b) as a function of the in-plane and out-of-plane (inset) strains. Theoretical T_C values in regards to the least strained value of S2000 film are given on the right hand scale of (b). The calculated magnetic moment is not shown in (a), because the changes were smaller than 1 %. [**P6**]

saturation magnetization and the Curie temperature are plotted against the in-plane and out-of-plane strain in figure 17 and this is compared with the theoretical calculations made with the Green's function method. For the details about the calculations see the reference [46] and [**P6**]. The experimental and theoretical results for the strain dependence of the T_C show very good agreement with a small increase with decreasing strain. Similar tendency is seen in the experimental M_s values, but the calculated magnetic moment is almost independent of the strain in this range and it is not shown in the figure. The larger change in the experimental T_C and M_s within the strain range, compared to the calculated ones, could be contributed by the possible changes in the amount of ASD and oxygen vacancies, which cannot be eliminated in real samples. Anyhow, the experimental T_C values of the both series are clearly lower than the T_C of the polycrystalline target used in their deposition or in other polycrystalline samples (410 K to 450 K [17]). Also, the theoretical M_s value of an optimal SFMO is almost twice as large as observed in the films of the thinner-film series.

The structural and magnetic properties of the films with different thicknesses from 50 nm to 500 nm indicate that the best quality films are obtained with the pulse number of 2000, which results in around 150 nm to 160 nm thick films. More structural defects and impurity phase are formed in thicker films and the strain effect has larger role in the thinner films. These investigations also show that the large difference between the polycrystalline bulk and thin film samples are not caused by the substrate induced strain. This difference is discussed more detail in the section 6.

5 The effect of substrate induced defects

The choice of substrate is very critical in the thin film fabrication, because the structure of the film depends on surface structure of the substrate. Also, a large enough difference in the lattice parameters could prevent the growth of the film and therefore, the substrate is usually chosen to have lattice parameters close to the desired film material. In spite of this, at least a small lattice mismatch between the film and the substrate exists with the exception of the homoepitaxial systems, where the film is grown on a substrate of same material. The lattice mismatch between the substrate and the grown material can be expressed with

$$\varepsilon_{\mathrm{M}} = \frac{a_{\mathrm{s}} - a_{\mathrm{m}}}{a_{\mathrm{m}}}, \tag{8}$$

where the a_{s} and a_{m} are the lattice parameters of the substrate and the grown material, respectively.

Like in many other complex magnetic oxides, the structure and structural defects have a significant role in the magnetic and electrical properties of SFMO. Therefore, it is expected that the properties are also highly dependent on the substrate. For example, the growth mechanism of SFMO has been seen to depend on the substrate and the saturation magnetization has been observed to decrease with increasing lattice mismatch [26, 95]. The effect of different lattice mismatches was investigated by growing SFMO thin films on $SrTiO_3$ (STO), $(LaAlO_3)_{0.3}(Sr_2AlTaO_6)_{0.7}$ (LSAT), $SrLaAlO_4$ (SLAO) and MgO single crystal substrates [**P5**]. These four samples in the AD-series are denoted as A-STO, B-LSAT, C-SLAO and D-MgO, respectively. Another two sets of films (A1- and B1-series) were grown at different atmospheres on STO, MgO and $NdGaO_3$ (NGO) substrates [**P3**]. However, only few aspects of their structural and magnetic properties are presented here. The main focus of the A1- and B1-series is in the magneto-transport properties, which is discussed in the section 7.

The lattice parameters of the used substrates and the mismatches between the substrates and bulk SFMO are presented in table 3. SFMO grows straight one unit cell over another on NGO. With other substrates, the SFMO in-plane lattice parameter a/b has a better match with the diagonal of the substrate basal planes, $\sqrt{2}a_{\mathrm{s}}$, than the $a_{\mathrm{s}}/b_{\mathrm{s}}$ parameter. Therefore, SFMO grows diagonally on these substrates and the lattice mismatch is obtained by replacing the a_{s} with the $\sqrt{2}a_{\mathrm{s}}$ in equation (8). Because the films have been grown at temperature well above room temperature, the thermal mismatches, $\varepsilon_{\mathrm{t}} = (\alpha_{\mathrm{SFMO}}\text{-}\alpha_{\mathrm{subst}})\Delta T$, were also determined and they are shown in table 3. The ε_{t} values were calculated using the temperature difference between T_{d} and room tem-

Table 3. The lattice constants of the substrates and the lattice mismatches between the SFMO and the substrates.

Substrate	a_s (Å)	b_s (Å)	c_s (Å)	$\sqrt{2}a_\mathrm{s}$ (Å)	ε_M (%)	ε_t (%)
STO	3.901	–	–	5.517	-1.05	0.29
LSAT	3.868	–	–	5.470	-1.88	0.60
SLAO	3.756	–	12.636	5.312	-4.71	0.41
MgO	4.214	–	–	5.964	6.97	0.00
NGO	5.430	5.500	7.711	–	-2.6/-1.3	0.31

perature together with the thermal expansion coefficient of the bulk SFMO, $\alpha_\mathrm{SFMO} = 14 \times 10^{-6}\,\mathrm{K}^{-1}$ [101], and the substrate α_subst. The thermal expansion coefficient values for the substrates vary a lot depending on the source, but here the substrate supplier values were used. The thermal mismatch values are rather small with all of the substrates and clearly smaller than the lattice mismatch. Therefore, its effect has been considered negligible in these investigations.

5.1 Structural properties

The good quality of the films was confirmed with standard XRD measurements. No indication of lattice mismatch related impurities or changes in texturing of the films were found. However, corresponding impurity phase peaks as in the S8 sample (section 4.1) were observed in the θ-2θ-scan of B1-series film on STO, which are more likely related to different deposition atmosphere. The lattice parameters of the films in the AD-series were determined from the (00l), (206), (336) and (404) peaks using the Nelson-Riley method, and for the films in A1- and B1-series from the (00l) and (204) peaks. The in- and out-of-plane strains (equation (7)) as well as the change in the unit cell volume, $\Delta V = (V_\mathrm{f} - V_\mathrm{b})/_\mathrm{b}$ were obtained by comparing the lattice parameters with the bulk values using same accuracy [100]. These values are presented in table 4.

The in-plane strains in the B1-series are larger and tensile, regardless of the lattice mismatch. Also, the change in the unit cell volume is significantly larger for the films in the B1-series, which were made in more reducting atmosphere. These indicate that the lengths of the lattice parameters in these films are more affected with the oxygen vacancies and other defects due to the more reducting deposition atmosphere than the substrate induced strain. As mentioned in the section 3.1, the deposition atmosphere was re-optimized after the A1- and B1-series and before the AD-series. Therefore, it is

Table 4. The main structural properties of the films on different substrates. [**P3**, **P5**]

Film	a (Å)	c (Å)	ΔV (%)	ε_a (%)	ε_c (%)	$\varepsilon_{\mathrm{WH}}$ (%)	ϕ-FWHM (°)	B_{ord}	ASD (%)	
A-STO	5.554	7.941	-0.15	-0.38	0.61	0.18	0.50	0.89	11	[†]
B-LSAT	5.592	7.885	0.52	0.31	-0.10	0.02	0.51	0.96	4	[†]
C-SLAO	5.596	7.870	0.46	0.37	-0.29	0.02	0.93	0.94	6	[†]
D-MgO	5.592	7.884	0.50	0.30	-0.11	0.01	0.79	0.80	20	[†]
A1-STO	5.52	7.96	-1.1	-1.1	0.9	–	0.45	–	–	[*]
A1-MgO	5.58	7.90	0.3	0.0	0.1	–	0.80	–	–	[*]
A1-NGO	5.57	7.89	-0.2	-0.2	0.0	–	0.69	–	–	[*]
B1-STO	5.69	7.97	5.2	2.0	1.0	–	0.51	–	–	[**]
B1-MgO	5.70	7.88	4.4	2.2	-0.1	–	0.71	–	–	[**]
B1-NGO	5.68	7.91	4.0	1.8	0.3	–	0.54	–	–	[**]

[†] Films made in 9 Pa pressure Ar atmosphere. Lattice parameters determined with Nelson-Riley method. [**P5**]

[*] Films made in 9 Pa pressure ArH_2(5 %). Lattice parameters determined from (00l) and (204) peaks. [**P3**]

[**] Films made in 11 Pa pressure ArH_2(5 %). Lattice parameters determined from (00l) and (204) peaks. [**P3**]

expected that less reducting atmosphere used for the AD-series leads to a difference in oxygen content compared to the A1-series and the strain values are not directly comparable. The a parameter of the A1-STO is exactly the same as the $\sqrt{2}a_{\mathrm{s}}$ of the STO substrate and the a parameter of the A1-MgO is the same as in bulk SFMO. This indicates that the A1-STO film is fully strained and the A1-MgO is fully relaxed, but that is not the case in the AD-series. The results presented in the section 4.1 also suggested that the films made on STO in more reductive ArH_2 atmosphere (thicker-film series) relax at higher thicknesses than the films made in Ar atmosphere (thinner-film series). This could be related to some additional defects or oxygen content. Nevertheless, the overall tendencies for the strains and the change in the unit cell volumes are similar in the A1- and AD-series.

A compressive in-plane strain was observed in A-STO and tensile in D-MgO, which are in good agreement with the strains in A1-series and with the lattice mismatches. However, the observed ε_a is tensile in B-LSAT and C-SLAO, despite the compressive mismatch. Also, the compressive in-plane strain in A1-NGO is rather small in the sense of the larger compressive mismatch compared to the STO. Due to the quite closely packed structure of SFMO, it is possible that large enough compressive mismatch cannot compress the structure enough. Instead, some interface defects could be formed, which relax the structure towards its bulk value or over-relax towards tensile strain. Thus, it seems that the compressive mismatch can be between the $-1\,\%$ to $-2\,\%$, in the range between STO and LSAT, before major structural defects or reorganization occur at the interface. The magnitudes of the in-plane strains in the films of AD-series do not show large variation, but the magnitude of the out-of-plane strain in the A-STO is clearly larger than in others. This is also seen in the change of the unit cell volume, which is clearly smaller for A-STO. These suggest that the elongation of the *c* parameter under compressive in-plane strain is easier than the compression under tensile in-plane strain. The length of the *c* parameter is also seen to be affected by the deposition parameters and structural defects [33, 94, 95], which was observed also in the A1- and B1-series. Therefore, it is clear that the substrate induced strain alone cannot explain the differences in ε_c and ΔV between the films in AD-series.

The microstrain, determined from the $(00l)$ peaks, describes the variation of the *c* parameter throughout the film thickness. In addition to the strain and relaxation of the lattice parameters, this variation could be caused by the horizontal defects like stacking faults. The $\varepsilon_{\mathrm{WH}}$ (table 4) was observed to be one order of magnitude larger in compressively strained A-STO when compared to the other films in AD-series. Because the out-of-plane strain and the change in the unit cell volume suggested easier elongation of the *c* parameter under compressive in-plane strain, the variation of the *c* parameter due to the relaxation is larger in compressively strained A-STO film, but it cannot rule out the possibility for higher stacking fault density. The ϕ-FWHM determined from the (204) peak is given in table 4 for all the films. The values show good consistency between the A1-, B1- and AD-series for the films grown on same substrate. The ϕ-FWHM is smallest around 0.5° for the films on STO and LSAT. In the films on NGO, the ϕ-FWHM is slightly larger and most dependent on the deposition atmosphere. The largest ϕ-FWHM is observed in the films on MgO and SLAO, around 0.8° and 0.9°, respectively. The ϕ broadening, with the instrumental width around 0.2° to 0.3°, suggests that all the films have some low angle grain boundaries. The low angle grain boundary density is largest in the C-SLAO films, in which the largest compressive mismatch resulted in tensile strained film. When compared to the films on STO, LSAT and NGO, the low angle grain boundary density is also larger in the films on MgO, which have the largest film/substrate mismatch. The B-site ordering was also determined for the films in AD-series and they are listed in table 4. The amount of ASD does not correlate with other structural properties like strain or ϕ-FWHM, but was found to be smaller in the cases where the compressive mismatch resulted in tensile strained films.

To investigate the interface defects and their dependence on the lattice mismatch more detail, a thorough TEM investigation was carried out on the films in the AD-series. The overall HRTEM images of all the films are shown in figure 18(a)-(d) and they reveal sharp film/substrate interface with some vertical defects, which are pointed out with the

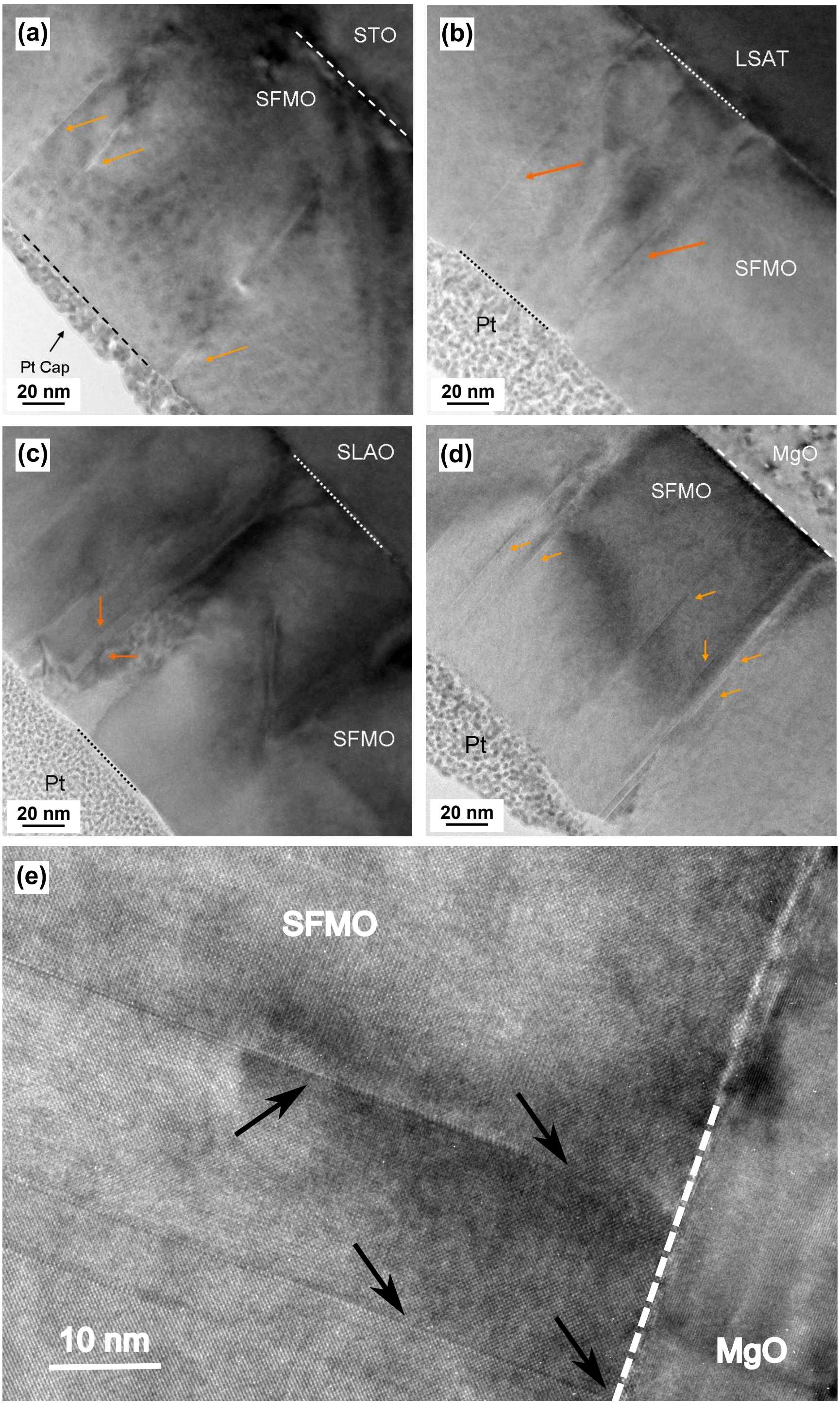

Figure 18. The HRTEM images of the (a) A-STO, (b) B-LSAT, (c) C-SLAO and (d) D-MgO in [100] viewing direction. The substrate/film interface is indicated with the dashed line and the vertical defects with the orange arrows. [**P5**]

orange arrows. In addition to the possible antiphase boundaries (figure 18(e)), it seems that at least some of these defects are threading dislocations related to the horizontal misfit dislocations at the interface, which is rather common strain relaxation mechanism in heteroepitaxial systems. Higher magnification HAADF STEM images of the A-STO and D-MgO films showing the threading dislocation are shown as an example in figure 19(a). A Fast Fourier Transform (FFT) filtered image of the SFMO/MgO interface, obtained using (200) reflections corresponding to the in-plane direction, shows several misfit dislocations at the interface. However, only some of these horizontal misfit dislocations result in vertical defects. As an example, a close-up of the interface in the D-MgO, with the details of the FFT filtered image showing the misfit dislocations, is shown in figure 19(b). In general, a larger mismatch causes more misfit dislocations, which lead to the observed threading dislocations. On the other hand, the threading dislocations are related to the low angle grain boundaries, which were confirmed by the XRD studies. The C-SLAO (figure 18(c)) and the D-MgO (figure 18(d)) have clearly more misfit dislocations and therefore, the density of low angle grain boundaries is also larger corresponding very well with the observed ϕ broadening. Earlier TEM investigations of the SFMO on STO have introduced the defect formation as a strain relaxation mechanism [94, 97] and our TEM and XRD results show that the defect concentration is higher with larger lattice mismatch. On this basis, it is clear that the SFMO lattice parameters relax through defect formation at least with higher lattice mismatches. The TEM images in figure 18 also indicate that the growth rate is smaller with LSAT substrate and the used 2000 pulses lead to film thickness of around 140 nm. With all other substrates the film thickness achieved with 2000 pulses is around 160 nm to 170 nm, which is very close to the value obtained by extrapolating the reflectivity results [**P6**].

The higher magnification HRTEM images were also taken from all the films in the AD-series and they are shown in figure 20(a)-(b) for the C-SLAO and D-MgO films. The horizontal stacking fault type defects together with the vertical antiphase boundaries or dislocations, which are visible in figure 20(a), were observed in both A-STO and C-SLAO samples. However, only vertical defects were observed in the B-LSAT and D-MgO samples as shown in figure 20(b). The horizontal defects could be the reason for increased microstrain and variation of the c parameter through the film, but the amount of these locally observed defects is not high enough to explain these differences. Furthermore, a parasitic particle in SFMO matrix is observed in D-MgO (figure 20(c)), which most likely belongs to the $SrMoO_4$ phase. The amount of this impurity is below the detection limit of XRD, because it was not observed in any of

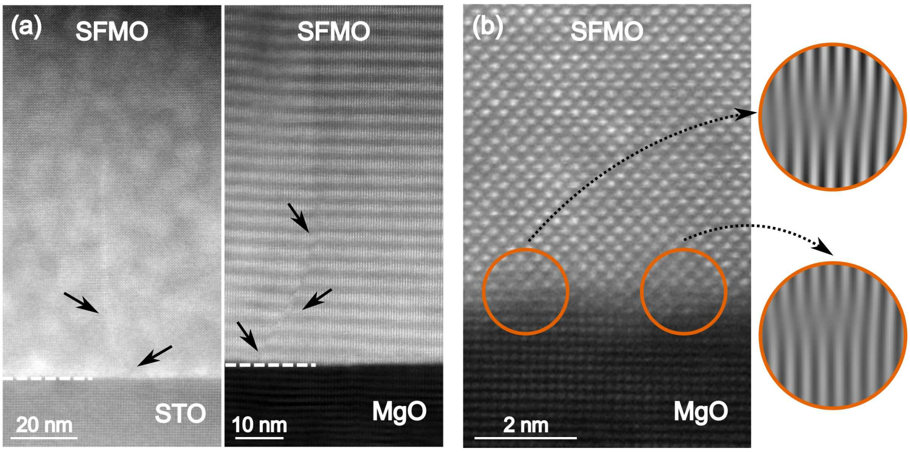

Figure 19. (a) The HAADF STEM images of the SFMO/STO and SFMO/MgO interfaces showing threading dislocation type defects, which are caused by vertical misfit dislocations at the interface. (b) The close-up of the SFMO/MgO interface with the details from the corresponding FFT filtered image showing the misfit dislocations. [**P5**]

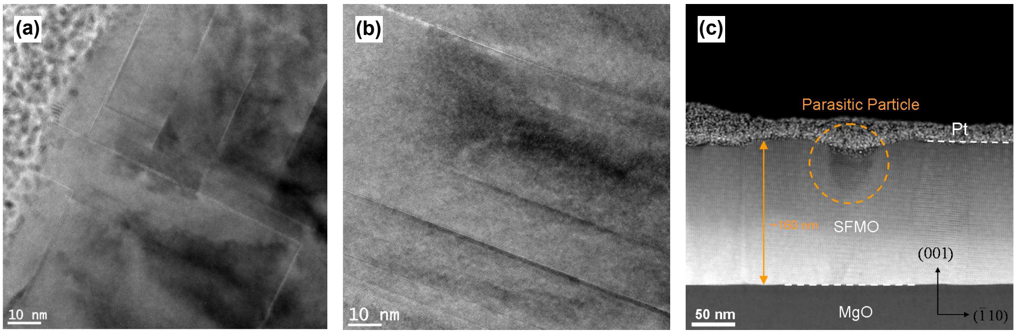

Figure 20. The higher magnification HRTEM images of (a) C-SLAO and (b) D-MgO taken at the same angle in relation to the substrate. (c) The HAADF STEM image of the D-MgO, which reveals the parasitic particle. [**P5**]

the XRD measurements. Even though similar parasitic phase has been seen in previous TEM investigations of SFMO films on STO [102], no parasitic particles were observed in any other films. The coherent interface between the SFMO matrix and the parasitic particle together with the largest lattice mismatch in D-MgO suggest that the formation of the parasitic particle is related to the growth process of the vaporized species induced by the large tensile strain.

5.2 Magnetic properties

The significant role of oxygen vacancies in the magnetic properties of SFMO has been undeniably proven by several theoretical studies and they all show reduction of M_s due to the increasing amount of oxygen vacancies [32, 37, 46]. Also, an increase in T_C with increasing amount of oxygen vacancies has been theoretically found and supported by our investigations with vacuum annealed SFMO thin film discussed in the section 6 [**P6**] [46]. In this sense, it is obvious that the magnetic properties of A1- and B1-series differ from the AD-series. Taking also into account that the measuring equipment and the determination of T_C were different for A1- and B1-series than for the AD-series, the comparison of the absolute values is not sensible. Furthermore, the highest and lowest onset T_C values within A1- and B1-series are both in films deposited on STO substrate and the M_s values of the B1-series are reduced from the A1-series (table 5). When this is considered in respect to the previous theoretical studies, which have also shown decrease of T_C and M_s due to increasing amount of ASD [32, 46], it seems that the amount of ASD is higher in B1-films indicating that deposition atmosphere has strong influence on the B-site ordering and on the amount of oxygen vacancies in SFMO films. Thereby, the structural defects due to the different deposition atmosphere might have stronger effect on the magnetic properties in A1- and B1-series than the lattice mismatch related effects.

The structural defects cause the formation and pinning of the domain walls, which might change the field response of the magnetization. In the results of the AD-series, a strong correlation between the shape of the hysteresis loops (figure 21(a)) and the lattice mismatch related defects, such as low angle grain boundaries, dislocations and stacking faults, were found. The shape of the $M(B)$ hysteresis curve for the A-STO, which has the lowest amount of defects, is as in typical ferromagnet with high remanence of 63 % of the saturation magnetization. On the other hand, the $M(B)$ hysteresis curve of the C-SLAO, which has the highest defect concentration, is significantly skewed with remanence being only 15 % of the M_s. This effect is also seen in the 100 mT magnetization

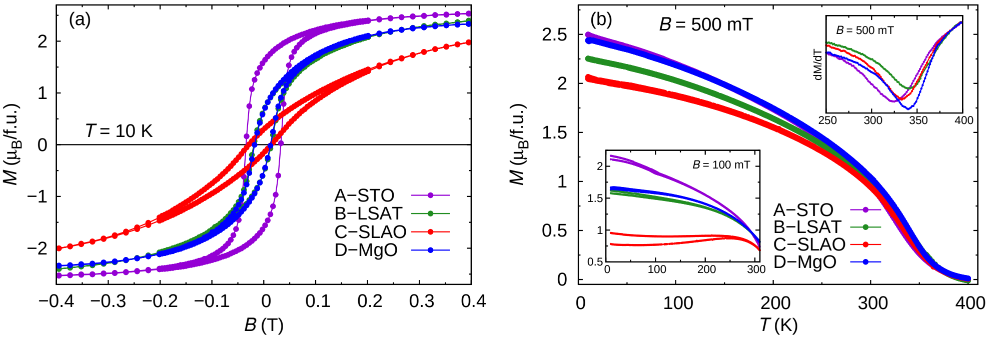

Figure 21. (a) The magnetization hysteresis loops at 10 K for the films in AD-series. (b) The temperature dependence of the magnetization in 500 mT. The bottom left inset shows the low temperature close-up of the ZFC and FC curves measured in 100 mT field. The top righ inset shows the temperature derivative of the magnetization in 500 mT used for the T_C determination. The effects of the substrate and the sample holder are subtracted from all the curves. [**P5**]

curves shown in the left inset of figure 21(b) as a large difference in the irreversibility *i.e.* in the deviation of the ZFC and FC curves. However, no irreversibility was observed in the magnetization curves measured in 500 mT field (figure 21(b)), because the field is large enough for saturation. Altogether, both the $M(B)$- and $M(T)$-curves confirm that the field required to modify and align domains in SFMO thin films depends on the density of lattice mismatch induced defects.

The field and temperature dependence of magnetization in figure 21 was also used to determine the Curie temperature, saturation magnetization, coercivity field, B_c, and remanence, M_r, of the films in AD-series and the values are shown in table 5 together with the T_C and M_s values of the A1- and B1-series. The M_r values correlate nicely with the skeweness of the hysteresis loop as mentioned before and no major differences were observed in the B_c despite its slightly larger value in A-STO. The changes in M_s observed within the AD-series were also small, but the M_s variation in the A1- and B1-series was clearly larger, which is most likely related to the defects induced by the different deposition atmosphere. The Curie temperatures of the tensile strained samples in the AD-series were also similar, but the values were clearly larger than in the compressively strained A-STO. In fact, all the values presented in table 5 for B-LSAT and D-MgO are surprisingly close to each other like the out-of-plane strains (table 4). Our results discussed in the section 4 showed with experiments and theoretical calculations

Table 5. The main magnetic properties of the films grown on different substrates. The M_s values for the films on NGO are not presented due to the dominance of paramagnetic effect from the substrate. [**P3**, **P5**]

Film	T_C (K)	M_s (μ_B/f.u.)	B_c (mT)	M_r (μ_B/f.u.)	
A-STO	324	2.54	34	1.61	†
B-LSAT	340	2.34	17	0.66	†
C-SLAO	335	2.00	21	0.30	†
D-MgO	337	2.33	15	0.65	†
A1-STO	375	2.62	–	–	*
A1-MgO	345	1.77	–	–	*
A1-NGO	325	–	–	–	*
B1-STO	290	2.03	–	–	*
B1-MgO	315	1.48	–	–	*
B1-NGO	330	–	–	–	*

†T_C determined from the 500 mT $M(T)$-curve. M_s, B_c and M_{irr} values given at 10 K. [**P5**]
*Onset T_C determined from the 100 mT $M(T)$-curve. M_s given at 5 K. [**P3**]

that the T_C and M_s values are slightly reduced with the elongation of the *c* axis and the decrease in T_C has also been observed before [33]. Based on these theoretical strain results, in which the other defects do not contribute, the change in the *c* axis length between the A-STO and B-LSAT could reduce the T_C by 5 K and M_s by 0.1 μ_B/f.u. Even though it seems that the the magnetic properties depend on the direction of the strain and the length of the *c* axis, the effect of the strain is not large enough to explain all the changes between the films on different substrates.

In order to clarify the role of different structural defects in magnetic properties of SFMO films grown on different substrates, the T_C and the M_s of the films in AD-series were plotted against the measured ASD and ϕ-FWHM (figure 22). Previously, the reduction of M_s and T_C has been connected to the increasing amount of ASD and the M_s have shown linear dependence with the ASD [26, 32, 34, 70, 86]. However, the measured ASD does not show any clear correlation with the M_s as can be seen in the inset of figure 22. Instead, the decreasing overall tendency of M_s with increasing ϕ-FWHM suggests that the other structural defects like low angle grain boundaries, dislocations and stacking faults overshadow the effect of ASD in the films grown on substrates with different lattice mismatches. Unlike the M_s, the T_C decreases linearly with ASD, if the D-MgO film is ignored as can be seen from the inset of figure 22. Moreover, the Curie

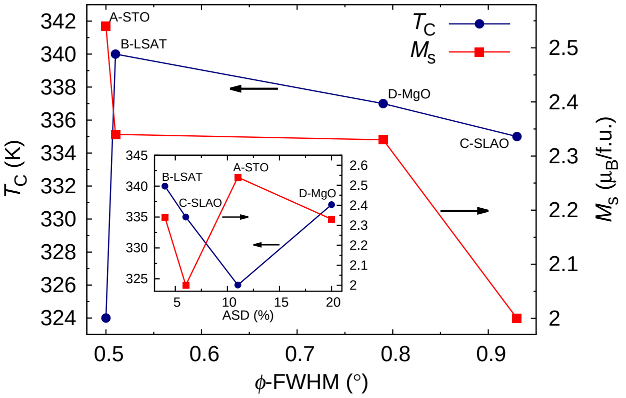

Figure 22. The Curie temperature (left hand scale) and the saturation magnetization (right hand scale) of the films in the AD-series as a function of ϕ-FWHM, which describes the amount of low angle grain boundaries. The inset shows the corresponding values as a function of ASD. The samples are labelled in the figure, because the ϕ-FWHM and the ASD do not correspond in the films. [**P5**]

temperature versus ϕ-FWHM in figure 22 shows a slight decrease in T_C with increasing amount of lattice mismatch related defects in tensile strained samples, but this cannot explain the lower T_C of A-STO. In order to understand the changes in T_C between tensile and compressively strained films, the oxygen vacancies need to be considered, even though their amount in these films cannot be confirmed. As mentioned before, strong evidence of the increase in T_C with increasing amount of oxygen vacancies has been shown. This suggest that the tensile strain and the lattice mismatch related defects can promote the formation of oxygen vacancies and cause the higher T_C of tensile strained films compared to the compressively strained A-STO. The higher amount of oxygen vacancies in tensile strained samples is also in good agreement with the observed saturation magnetizations.

Altogether, the results for A1- and B1-series show that SFMO films are very sensitive to the deposition atmosphere, which presumably affects at least the amount of oxygen vacancies in the films, but can also cause other structural defects. In addition to the deposition atmosphere, the magnetic properties of SFMO films are highly dependent on the choice of substrate through lattice mismatch induced structural defects. The low angle grain boundaries, dislocations and stacking faults cause the formation and pinning of the domain walls as well as could promote the formation of oxygen vacancies.

Also, the observed ASD has a reducing effect on the T_C and M_s of SFMO thin films, but like the effect of substrate induced strain, it is outshined by the larger effect of interface defects. Hence, the choice of a substrate is an extremely important factor that needs to be considered in the fabrication of SFMO thin films for novel applications. Based on these results, best structural properties are achieved with STO substrate and aside from T_C, the best magnetic properties are also obtained by growing SFMO on STO.

6 The effect of ASD and oxygen vacancies

The magnetic properties of the SFMO thin film and polycrystalline bulk samples differ significantly from each other. The Curie temperature of the polycrystalline target used in the film deposition is around 23 % higher than in the SFMO films. On the other hand, the saturation magnetizations of the films are clearly lower than the theoretical value of $4\,\mu_\mathrm{B}$/f.u., but around 33 % higher than in the target. To have SFMO based spintronic devices in the future, it is clear that the magnetic properties, especially the T_C, of the films need to be improved. Even though, the external factors such as the substrate induced strain or lattice mismatch related defects discussed in the preceding sections clearly have some influence on the magnetic properties, they cannot explain these differences. Therefore, the effect of intrinsic defects, ASD and oxygen vacancies ($\mathrm{V_O}$) need to be also considered.

Several earlier theoretical and experimental studies have shown clear connection between the magnetic properties of SFMO and the anti-site disorder. The saturation magnetization has been seen to decrease with increasing amount of ASD [24, 32, 33, 35, 40, 46, 81, 86, 103, 104]. Similarly, a decrease in the Curie temperature of SFMO has been seen [32, 35, 46, 103]. However, Huang *et al.* have observed an increase in T_C with small amount of ASD after which a decreasing tendency is observed [104]. The number of reports about the effect of oxygen vacancies, especially on the T_C, is more limited and partly inconsistent. Strong theoretical and experimental evidence of the decreasing tendency of M_s with increasing number of oxygen vacancies has presented [24, 32, 105, 106], but experimental study has suggested a decrease also in T_C whereas theoretical investigations show increase in T_C with increasing amount of oxygen vacancies [46, 107]. In addition to the T_C and M_s, oxygen vacancies and ASD reduce the band gap in the majority spin channel. In case of ASD, this effect is large enough that the half metallic feature of SFMO is lost [36–39, 108]. However, the half metallic character is preserved with oxygen vacancies at least for small concentrations whereas the results are contradictory for larger concentrations [37–39, 109].

To estimate the changes in the amount of defects between SFMO films and bulks, the formation energies, E_form, of different ASD and oxygen vacancy configurations (figure 23) were calculated with the in-plane lattice constants of both SFMO and the commonly used STO substrate. The details of the calculations are given in [**P6**, SI]. The formation energies of the defects increase with the $-1.05\,\%$ compression of a, which would mean that it is more probable to have ASD and oxygen vacancies in the unstrained bulk sample than in the film compressed by the small negative lattice mismatch.

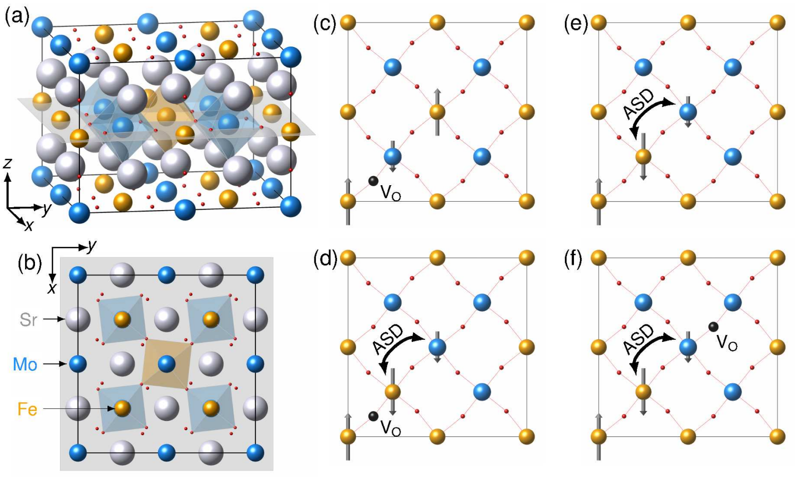

Figure 23. (a)-(b) The supercell of 8 f.u. of SFMO used in the calculations. (c)-(f) Schematic picture of the simulated defect configurations in the formation energy calculations. [**P6**, SI]

The fabrication temperature and atmosphere will also affect the formation of oxygen vacancies as can be seen in figure S4 of [**P6**, SI]. The exact oxygen partial pressures in the fabrication processes of thin film and bulk samples are impossible to determine, but their difference in film and bulk sample fabrication should be rather small. Therefore, the differences in the formation energies due to the strain can be considered as a good estimation for the formation probability of oxygen vacancies in these two sample types.

The ASD induced changes were experimentally clarified by determining the B-site ordering, B_{ord}, of the target and the standard 2000 pulses film. The B-site ordering of the film was determined as explained in the section 2.2. The B_{ord} of the target was obtained with the Rietveld refinement using the Maud program [110]. The overall $\theta - 2\theta$ scan was refined by allowing the Fe(Mo) ions occupy the anti-site *i.e.* Mo(Fe) positions and keeping the total number of Fe and Mo ions equal. The ASD of the film is around (12 ± 3) % whereas the ASD of the target is almost twice as high, around 28 %, which is in good agreement with the E_{form} calculations. Based on the earlier theoretical results [46], both T_{C} and M_{s} decrease with increasing amount of ASD up to 15 %. However, this range does not cover the ASD concentration of the target and additional calculations were made with a supercell containing 25 % of ASD. These imply that the decreasing tendency of T_{C} changes to increasing tendency when the amount of ASD is increased further [**P6**]. In this sense, the T_{C} of the films with 12 % of ASD is lower and the T_{C} of target with 28 % of ASD is higher than in the sample with the perfect B-site ordering. Although, this suggest that the T_C of SFMO could be improved with ASD in amounts higher than15 %, the density of state (DOS) calculations (figure 24(c)) show that the half metallic character is lost due to the additional states at the Fermi energy arising from the Mo at Fe position. This confirms that the amount of ASD should be further decreased in SFMO thin films to achieve samples with higher T_C, M_s and spin polarization, which all are desired for applications.

The earlier theoretical calculations have also predicted an increase in T_C and decrease in M_s with increasing amount of oxygen vacancies [46]. The formation energy calculations also suggested that the oxygen vacancies are more probable in the unstrained target. Therefore, the larger T_C could be also related to the higher amount of oxygen vacancies. To experimentally investigate the effect of oxygen vacancies, the standard 2000 pulses film (pristine) was annealed in ultra high vacuum conditions at 650 °C for 120 min (annealed). The oxygen concentration was investigated with HAXPES and the valence spectra of the pristine and annealed samples are shown in figure 24(b) and the calculated DOS in figure 24(c). The defect free case and the case with 8 % of oxygen vacancies were considered in the calculations and the details are given in [**P6**]. The structures between 0 eV and 2 eV binding energies arise from the Fe 3*d* and Mo 4*d* states. A shift of these features towards lower energy is observed in the DOS when 8 % of oxygen vacancies are introduced to the system. Correspondingly, a shift of these features towards higher binding energies is observed in the valence spectra of annealed sample. At the same time, the binding energies of the Mo 3*d*, Sr 3*d* and O 1*s* spectra are increased. Similar shift due to the increasing amount of oxygen vacancies are observed in the O 1*s* and Sr 3*d* spectra of $SrFeO_x$ and $SrTiO_3$ [111, 112]. Therefore, it is reasonable to expect that oxygen vacancies can be induced to the SFMO film by ultra high vacuum annealing and that the oxygen concentration is lower in the annealed sample.

The lattice parameters were determined from the pristine and annealed samples with XRD as for the thinner-film series in section 4.1. The obtained *a* parameter increased 0.3 % and the *c* parameter decreased 0.1 % with the annealing treatment. The temperature dependence of the magnetization near the ferro-paramagnetic transition is shown in figure 24(a) for the pristine and vacuum annealed samples. This was used to obtain the Curie temperatures as the minimum of the $\mathrm{d}M/\mathrm{d}T$ curves and around 20 K increase as a result of vacuum annealing was observed. Also, the saturation magnetization, which was determined from the $M(B)$ hysteresis curve, decreased by 0.2 μ_B/f.u. with vacuum

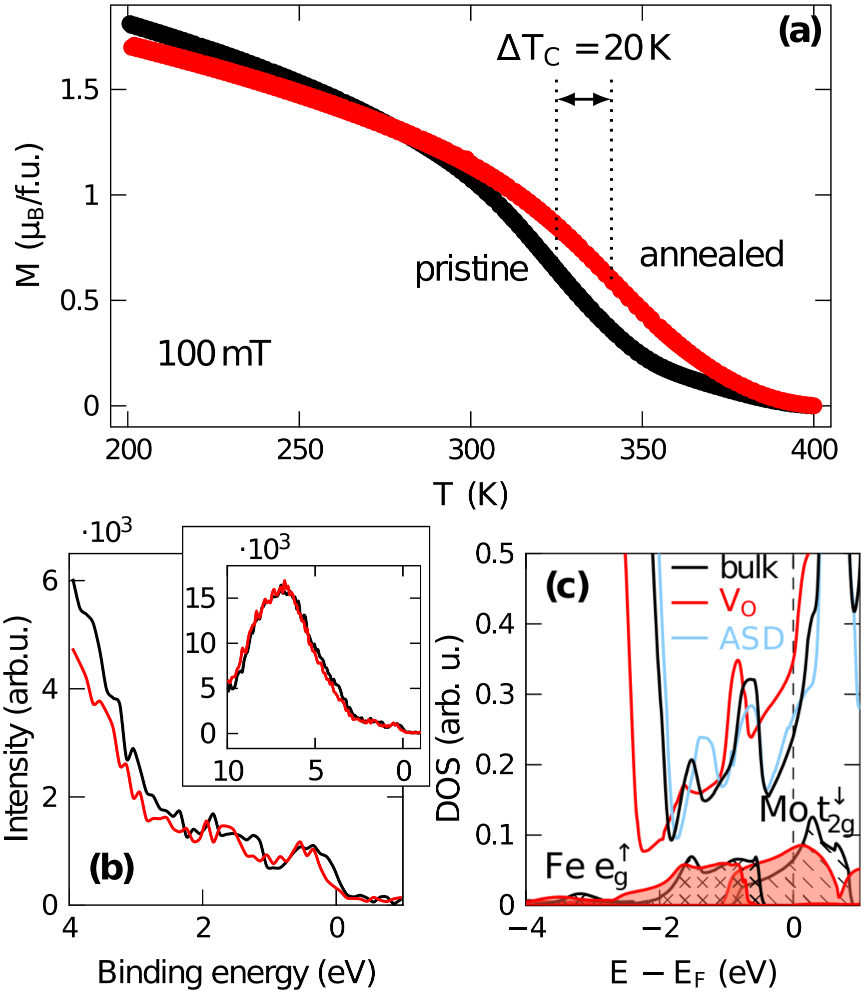

Figure 24. (a) The temperature dependence of magnetization for the pristine and annealed sample near the ferro-paramagnetic transition. (b) The XPS valence spectra of the pristine and annealed sample at room temperature. (c) The calculated DOS for the perfect SFMO and for SFMO with defects. [**P6**]

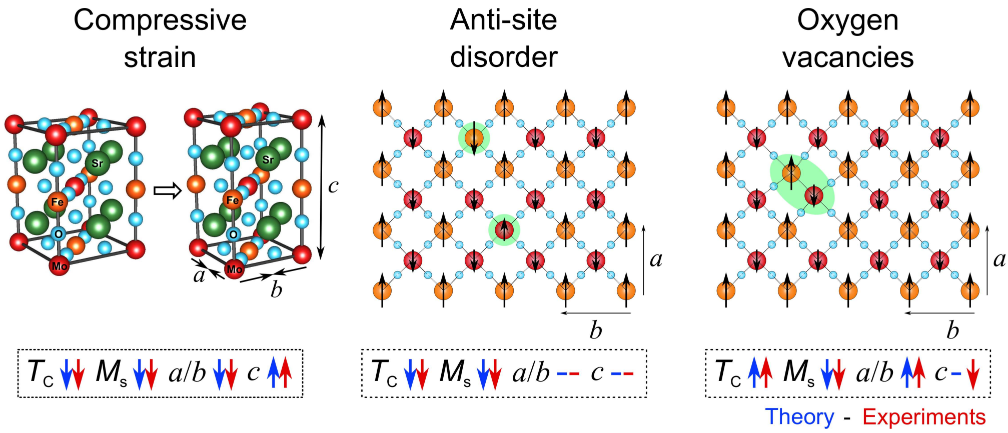

Figure 25. A schematic figure presenting the effect of strain, ASD and oxygen vacancies in SFMO. The results from theoretical calculations are shown in blue and from the experiments in red. [**P6**]

annealing. These changes suggest that the amount of oxygen vacancies is indeed increased as a result of vacuum annealing and that the oxygen vacancies increase T_C and decrease M_s as was expected from the calculations. Furthermore, the changes in the amount of ASD between the pristine and annealed sample are within the normal variation and do not contribute to the observed changes.

The difference in magnetic properties in SFMO thin films and polycrystalline bulks are clearly caused by a combination of different mechanisms. Even though the substrate induced strain itself does not have notable contribution to the magnetic properties of SFMO, it affects the formation probability of ASD and oxygen vacancies, which are the main mechanisms behind the differences in magnetic properties. The effect of strain, ASD and oxygen vacancies are summarized in figure 25 from the theoretical and experimental point of view. The theoretical results used, which are not included in [**P6**], are based on the study of M. Hoffmann *et al.* [46]. The experimental and theoretical results are in good agreement. They both suggest a decrease in M_s due to these defects, whereas the effect on the Curie temperature is increasing with oxygen vacancies and high ASD concentration over 15 %, but decreasing with low ASD concentrations. Therefore, the T_C of SFMO thin films could be improved by increasing the amount of oxygen vacancies, which should not destroy the half metallic character essential for applications, but definitely reduces the M_s. However, reducing the amount of ASD from the observed 12 % would also increase the T_C of the SFMO films and it is even necessary in order to maintain the high spin polarization, because the ASD has strong deteriorating effect on the half metallic feature of SFMO. Therefore, the first priority in the future investigations should be the improvement of the B-site ordering, which could be possibly achieved by optimizing the deposition process, especially the deposition temperature and the *in situ* annealing, further.

7 Magneto-transport in SFMO thin films

7.1 Temperature dependence of resistivity

The temperature dependence of resistivity in SFMO thin films usually show metallic behaviour at higher temperatures and an upturn in resistivity at low temperatures [23, 51]. Similar behaviour is also observed in our thin film samples. The resistivity of mixed valence manganites, which have similar properties with SFMO, can be described with relations like

$$\rho = \rho_0 + \rho_2 T^2, \tag{9}$$

$$\rho = \rho_0 + \rho_2 T^2 + \rho_{4.5} T^{4.5}, \tag{10}$$

$$\rho = \rho_0 + \rho_{2.5} T^{2.5}, \tag{11}$$

where the ρ_0 is the resistivity due to the impurity scattering [113, 114]. $\rho_2 T^2$ arises from electron-electron scattering [114, 115], $\rho_{4.5} T^{4.5}$ is related to the electron-magnon scattering or spin wave scattering [114, 115] and $\rho_{2.5} T^{2.5}$ corresponds to the combination of electron-electron scattering, electron-phonon scattering and electron-magnon scattering [113, 116]. In order to understand the resistivity mechanism in SFMO thin films, these equations were fitted to the metallic part of the $\rho(T)$-curves and this is shown for a measured example data in figure 26(a). The insets show the close-up of the fits in the low and high temperature points where the fits deviates from the data. All the fits follow the measured data quite nicely at the inspected temperature range, which eliminates the possibility to separate the dominating scattering mechanism. However, the right inset of figure 26(a) shows that the equation (9) agrees better with the measured data above 300 K than the equations (10) and (11). Thus, it seems that the electron-electron scattering can have significant contribution to the resistivity in the metallic regime of SFMO thin films. Nevertheless, none of these models fits to the $\rho(T)$-curves at the whole temperature range and it is obvious that the traditional resistivity-temperature mechanism does not completely explain the temperature dependence of resistivity in SFMO thin films.

In order to clarify the resistivity behaviour of SFMO thin films, we have introduced a semiempirical model of two spin channel system. Due to the half-metallicity, SFMO band structure has a gap in the majority spin band and density of states in the minority spin band, which means that it can be considered as a system with two spin channels connected in parallel [17, 41, 42, 49, 117, 118]. The band gap in the majority spin band could be reduced due to the oxygen vacancies, ASD and substrate induced strain [37, 38,

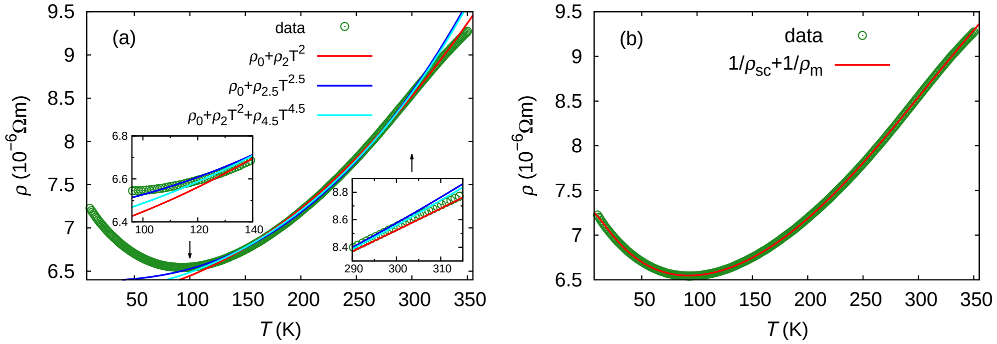

Figure 26. Fitting of (a) the traditional $\rho(T)$ relations (equations (9)-(11)) and (b) the model for a two spin channel system (equation (12)) to the measured example data of SFMO film on MgO. [**P3**]

40, 46, 94], which suggest that the band gap in SFMO thin films could be small enough that the temperature can excite electrons to the conduction band. Therefore, the spin up channel can be considered semiconductive whereas the spin down channel is metallic. The total resistivity of SFMO thin film is then formed by the resistivity of metallic spin channel (ρ_m), resistivity of semiconductive spin channel (ρ_sc) and resistivity from impurities and defects, which can be described by

$$\frac{1}{\rho_\mathrm{tot}} = \frac{1}{\rho_\mathrm{sc}} + \frac{1}{\rho_\mathrm{m}}. \tag{12}$$

The temperature dependence of resistivity in the semiconductive spin channel can be described by

$$\rho_\mathrm{sc} = \rho_\mathrm{d}^\mathrm{sc} \mathrm{e}^{E_\mathrm{g}/k_\mathrm{B}T} + \rho_0^\mathrm{sc}, \tag{13}$$

where the $\rho_\mathrm{d}^\mathrm{sc}$ is a constant related to the electrical charge density, ρ_d^0 is a temperature independent constant caused by the impurities and the E_g is the energy gap of the semiconductor. To describe the metallic part of the the total resistivity, all three equations (9)-(11) were fitted within this model to the measured data. It was found that the equation (10) together with ρ_sc has the best correspondence with our measured data. The fitting of the two spin channel system using equation (12) with equations (13) and (10) is shown in figure 26(b) for an example data.

The model of two spin channel system was developed within the investigations of the magneto-transport properties of two set of films grown on different substrates with different deposition atmospheres. The structural and magnetic properties of these films

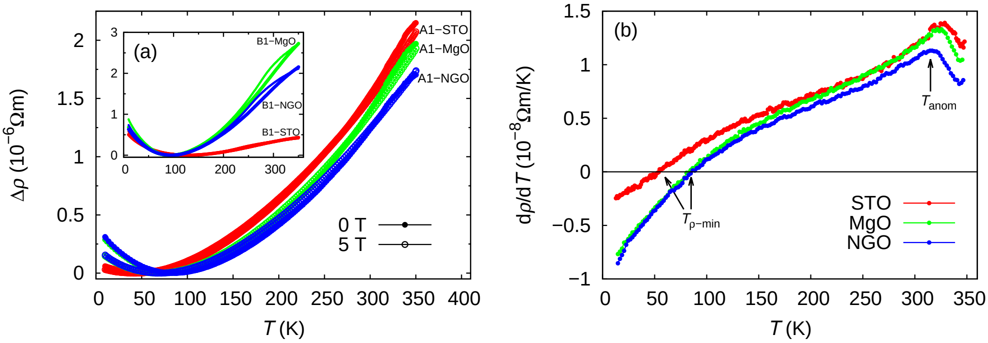

Figure 27. (a) The temperature dependence of the change in resistivity for the A1-films in 0 T and 5 T fields. The inset shows the corresponding dependency for the B1-films. (b) The temperature derivative of the resistivity in the 50 mT field for the A1-films. [**P3**]

are briefly presented in the section 5 and they are referred as A1- and B1-series. The change of the resistivity, $\Delta\rho$=$\rho(T)$-ρ_{min}, as a function of temperature in 0 T and 5 T fields are shown in figure 27(a) for samples in both A1- and B1-series. All the curves show metallic resistivity with semiconductive upturn at low temperature. The upturn is clearly larger in B1-films and only slight upturn is observed in A1-STO. Also, a small anomaly near 300 K is seen, which is reduced with applied magnetic field. To analyze the curves further, the temperature derivative of the resistivity (figure 27(b)) was used to determine the resistivity-anomaly (T_{anom}) and the resistivity-minimum ($T_{\rho-\mathrm{min}}$), which are listed in table 6. The T_{anom} seems to be related to T_{C} of the samples. Even though the absolute temperature value of the anomaly is smaller than the onset T_{C}, it has similar tendency and it is very close to the temperature of the midpart of the ferro-paramagnetic transition. The $T_{\rho-\mathrm{min}}$ as well as the low temperature upturn are clearly related to structural disorder of the films, because larger upturn and $T_{\rho-\mathrm{min}}$ values are observed in the films with weakest structural and magnetic properties (see section 5).

The equation (12) was fitted to the $\rho(T)$-curves of the A1- and B1-films. In every case, the fit followed the measured data in the whole temperature range. However, the fitting was inconvenient for A1-STO due the smallest low temperature upturn. The energy gap, E_{g}, of the semiconductive spin channel was determined from the fitting parameters. The E_{g} values are shown in table 6 and aside from the films on NGO, they are larger in the A1-series than in the B1-series correlating nicely with the $T_{\rho-\mathrm{min}}$ values and with the magnitude of the upturn. The larger E_{g} values in A1-films, especially in the films on STO, indicate that the structural defects, which deteriorate the magnetic

Table 6. The main resistivity properties of the films in A1- and B1-series. [**P3**]

Film	T_{anom} (K)	$T_{\rho-\mathrm{min}}$ (K)	E_{g} (meV)	T_{C} (K)
A1-STO	333	50	47.3	375
A1-MgO	325	77	7.3	345
A1-NGO	319	79	6.3	325
B1-STO	236	127	2.8	290
B1-Mgo	280	96	6.7	315
B1-NGO	258	94	6.7	330

properties, also reduce the energy gap and increase the semiconductive upturn. This means that in high quality films with better magnetic properties, the metallic spin channel is dominant and the semiconductive spin channel is recessive. This allows expecting that in extremely good SFMO films, the energy gap is so large that the metallic channel transport all the current and the low temperature upturn disappears.

The effect of vacuum annealing (section 3.2) and film thickness (thicker-film series in section 4) on the transport properties of SFMO films were also investigated. The change in the resistivity as a function of temperature is shown in figure 28(a) for the as-deposited film and the film vacuum annealed at 700 °C. The temperature dependence of the resistivity is shown in the inset. These figures clearly show that the resistivity and the low temperature upturn is increased as a result of vacuum annealing, even though no changes were observed in the magnetic properties aside from the increased paramagnetic moment above Curie temperature. Hence, the reduction of the semiconductive energy gap, observed as a larger low temperature upturn in vacuum annealed film, is most likely related to the increased amount of unidentified magnetic impurity. Also, a small anomaly near 250 K is seen in the 0 T curve of the vacuum annealed sample. Later investigations have suggested that it is related to the magnetic history of the sample, but the whole principle has not yet been clarified.

The temperature dependence of the change in resistivity for the film in thicker-film series (see section 4) is shown in figure 28(b). The figure clearly shows that the resistivity behaviour is dramatically changed when the film thickness is increased from the 150 nm to 270 nm, but no remarkable changes are observed with increasing the thickness further. The change in the resistivity at the whole temperature range is larger in the thinnest S2-film. Also, the resistivity at 10 K as well as the low temperature

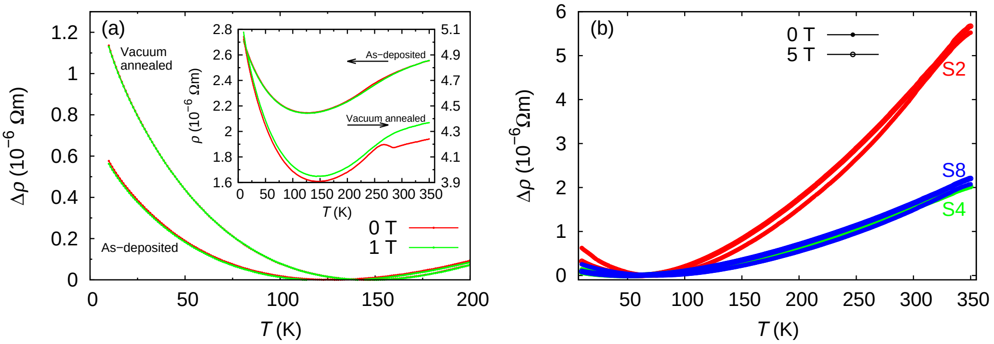

Figure 28. (a) The temperature dependence of the change in resistivity in 0 T and 1 T fields for the as-deposited and vacuum annealed samples. The inset shows the temperature dependence of the resistivity for the same samples. (b) The temperature dependence of the change in resistivity for the films with different thicknesses in 0 T and 5 T fields. The inset shows the magnetoresistivity as a function of temperature for the same samples in 1 T and 5 T fields. [**P2**, **P4**]

upturn are reduced by increasing the thickness. Earlier investigations have shown that strain reduces the band gap in the majority spin band [94], which would mean that the energy gap is smaller with larger strain. According to the XRD results (section 4.1), the thinnest S2-film is more strained than the thicker S4- and S8-samples, which would explain the observed larger low temperature upturn in resistivity of S2-sample.

Altogether, the temperature dependence of resistivity seems to be dominated by the structural defects that reduce the band gap in the majority spin band, enabling the thermal excitation of the electrons to the conduction band. This is seen in $\rho(T)$-curves as semiconductive type low temperature upturn, magnitude of which seems to be highly dependent on the structural properties like the amount of ASD, oxygen vacancies and substrate induced strain. Moreover, the model of two spin channel system appears to be effective way to clarify the resistivity-temperature behaviour of SFMO thin films, that does not follow any traditional models.

7.2 Magnetoresistance

The resistivity of SFMO thin films decreases with applied magnetic field in both polycrystalline and thin film samples [27–29, 51, 56, 58, 61, 119]. The phenomenon is clearly larger in granular samples like bulks and polycrystalline thin films [27, 56, 61].

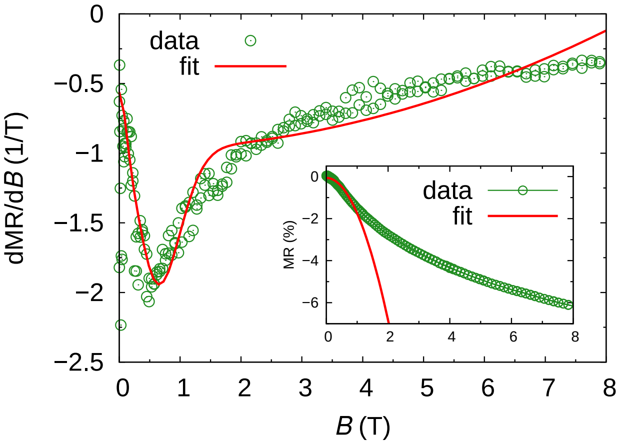

Figure 29. Fitting of the magnetoresistance model of granular polycrystalline materials (equation (14)) to the example data. The inset shows the fitting of metallic and semiconductive B^2 dependence to the example data of SFMO film on MgO. [**P3**]

The resistance of granular polycrystalline colossal magnetoresistive materials consists mainly of the scattering from nonmagnetic defects and phonons (R_0), spin polarized tunneling ($R_{\text{spt}}(B)$) and reduction of spin fluctuation (R_{int}) [53]. This can be described by [53]

$$\frac{\mathrm{d(MR)}}{\mathrm{d}B} = \alpha_1 \exp(-\beta_1 B^2) + \gamma_1 B^2 \exp(-\delta_1 B^2) - J - 3KB^2, \tag{14}$$

where the $\alpha_1, \beta_1, \gamma_1, J$ and K are fitting parameters. Because the MR phenomena in SFMO thin films has not been explained before, this model as well as the B^2 dependency due to the cyclotron motion of electrons were fitted to the example data of SFMO thin film (figure 29). This was done in order to deepen the understanding of the MR in SFMO thin films, even though the thin films are not granular. Neither this model nor the B^2 dependency follow the experimental data well enough and this allow us to exclude the spin polarized tunneling, reduction of spin fluctuation and the cyclotron motion of the electrons as a main MR mechanism. Instead, it was found that the MR has $\sqrt{B}$ dependency in high fields above 3 T and in the metallic regime below the T_C, which has previously been related to electron-electron interaction [120, 121]. In this high field regime, but in semiconductive temperature range, the dependency is changed from $\sqrt{B}$ to $B^{0.1}$. The MR in low field was found to be more dependent on the structural defects like low angle grain boundaries. The low field magnetoresistance (LFMR) of manganites arises from spin polarized tunneling between FM grains and this can be

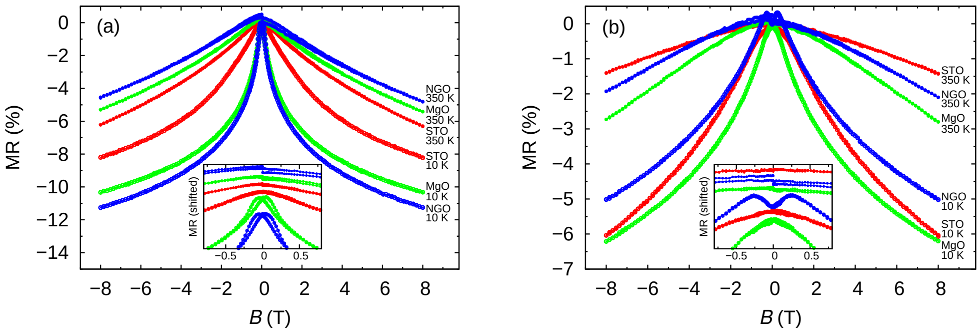

Figure 30. Magnetoresistance as a function of the magnetic field for (a) A1-films and (b) B1-films on different substrates at 10 K and 350 K. The insets show an enlargement of the curves in low field and the curves in it are shifted for clarity. [**P3**]

described with MR $\sim -A(M/M_\mathrm{s})^2$ [122]. However, this model does not fit to the LFMR observed in SFMO films, even though, the LFMR appears together with higher amount of low angle grain boundaries indicating that the LFMR in SFMO films is also due to the grain boundary tunneling.

The magnetic field dependence of magnetoresistance, obtained using equation (5), for the films in A1- and B1-series (section 5) are shown in figure 30. The negative MR in A1-samples is almost twice as large as in B1-films whereas the zero field resistivity at 10 K was observed to be smaller. This is most likely related to the better B-site ordering of the A1-films as suggested by the magnetic properties of the samples. In that case, the B1-samples should have more antiferromagnetically ordered anti-site domains, which increase the zero field resistivity. Even though the ASD induces negative MR in SFMO due to the suppression of the spin disorder close to the anti-site domains under applied magnetic field, the negative MR is also reduced if the amount of ASD is high enough, because it also reduces the spin polarization of the sample [33, 36]. In this sense, the smaller negative MR in B1-films is in good agreement with the resistivity-temperature results which showed larger low temperature upturn and smaller energy gap in the majority spin band for the B1-films indicating lower spin polarization. However, this cannot explain the whole phenomena. The lower M_s value of the B1-MgO (see table 5) indicate that the A1-STO has better B-site ordering than B1-MgO, but the negative MR and the energy gap are larger in B1-MgO. This could be related to the higher amount of low angle grain boundaries, which would enhance the tunneling MR effect in B1-MgO. The effect of low angle grain boundaries is also seen in the insets

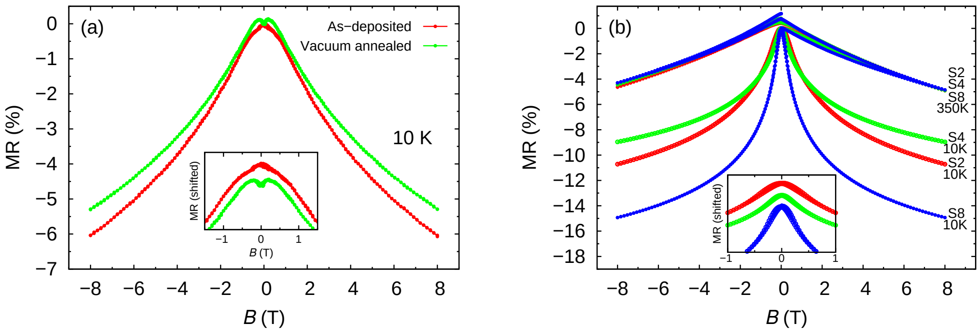

Figure 31. Magnetoresistance as a function of the magnetic field (a) for as-deposited film and film vacuum annealed at 700 °C at 10 K and (b) for the films with different thicknesses 10 K and 350 K. The insets show an enlargement of the 10 K curves in low field and the curves are shifted for clarity. [**P2**, **P4**]

of figure 30 as an rising LFMR effect in the films on NGO and MgO, which have the larger ϕ-FWHM values (see table 4).

The effect of vacuum annealing on the magnetoresistance of SFMO thin films is shown in figure 31(a). The negative MR is reduced as a result of the vacuum treatment, which is expected due to the increase observed in the low temperature upturn in $\rho(T)$-curves. Also, a small low field anomaly appears after the vacuum annealing as can be seen in the inset of figure 31(a). This LFMR effect is most likely related to the structural changes in the film, which causes also the increase in the lattice parameter lengths observed in the structural results (see section 3.2). It seems that these structural changes also deteriorate the spin polarization of the sample and cause the decrease in the negative MR.

The magnetic field dependence of MR showing the effect of film thickness is presented in figure 31(b). At 350 K, no changes are observed between the curves, because it is in the vicinity of the ferro-paramagnetic transition. However, the negative MR at 10 K is clearly increased by increasing the thickness from 270 nm to 500 nm and also the shape of the curve is changed especially in the low field part (inset of figure 31(b)). The theoretical calculations have shown that the band gap in the majority spin band is reduced due to the strain [94], which corresponds nicely with our observation that the low temperature upturn is larger in thinnest and most strained S2-film. Thus, it seems that the MR in SFMO films is reduced by the substrate induced strain due to the reduction of the spin polarization. On the other hand, the change in the low field part of the MR curve indicates that the same magneto-transport mechanism is not dominant at the whole thickness range. This can be related to the difference in the amount of low angle grain boundaries, which are more dominant in the thickest film and enhance the tunneling type LFMR.

All these results indicate, that the magnetoresistance of SFMO thin films is strongly related to the width of the band gap in the majority spin channel, which affects the spin polarization of the sample. When the spin polarization is reduced, the magnetic field response loses its magnitude and the negative MR effect is smaller. On the other hand, the MR in low field was enhanced with the larger amount of low angle grain boundaries and indications about the effect of lattice mismatch related defects on the shape of the MR curve were also found. Therefore, it is clear that the MR phenomenon in SFMO thin films is a superposition of different mechanism, which all appear to be related to the structural changes in the films. It is evident, that further investigations are required to fully understand the complex magneto-transport phenomena in SFMO thin films.

8 Conclusions

In this thesis, the magnetic properties and magnetoresistivity in SFMO thin films with wide range of different structural properties and defects were systematically studied and the growth process for pulsed laser deposited SFMO thin films were optimized. The SFMO was found to be very sensitive to the deposition atmosphere and the best films with the used equipment were grown in 9 Pa pressure Ar atmosphere. Also, rather high temperatures are required to grow high quality SFMO films and the optimal deposition temperature was found to be 1050 °C. The *ex situ* post-annealing treatments carried out in Ar, ArH_2(5 %), air and vacuum conditions were not sufficient to improve the magnetic properties of the SFMO films aside from the treatments in ultra high vacuum.

The effect of strain and film thickness was investigated by growing SFMO films on STO substrate with different pulse numbers corresponding thickness range from 50 nm to 500 nm. The best structural and magnetic properties were obtained with the film thickness around 150 nm. More structural defects and impurities were observed with higher thicknesses, without any improvement on the magnetic properties. Even though only slight decrease in T_C and M_s were observed with increasing strain or decreasing thickness, the strain effect has a larger role in thinner films.

The substrate dependent properties were studied by growing the films on five different single crystal substrates with different lattice mismatches. The used substrates were STO, LSAT, SLAO, MgO and NGO. The large enough compressive mismatch around 1 % to 2 % was found to result in smaller compressive strain than expected or tensile strain. This implies that the amount of compression in quite closely packed SFMO structure is limited and some interface defects or re-organization at the interface occur instead. The magnetic properties were also found to be highly dependent on the substrate, because of the lattice mismatch induced defects. These cause the formation and pinning of the domain walls and could enhance the formation of oxygen vacancies. The reducing effect of the observed ASD was also overshadowed by the dominance of these substrate induced defects, which could be best avoided by using the STO substrate.

The effect of ASD and oxygen vacancies was experimentally investigated by determining the amount of ASD in different types of samples and annealing the film in ultra high vacuum conditions. This was done in order to improve the T_C of the films and understand the mechanisms behind the different magnetic properties of SFMO thin film and bulk samples. With formation energy calculations, the formation of these defects was found to be more likely in unstrained bulk samples than in slightly compressively strained films. Consistently, the amount of ASD was found to be twice as large in the target used in the deposition than in the films. The oxygen vacancy results also suggested a larger amount of vacancies in the target and confirmed the earlier theoretical prediction about the increase of T_C with increasing amount of oxygen vacancies. The experimental findings of this work together with the present and earlier theoretical results indicate that the T_C of SFMO thin films could be improved by increasing the amount of oxygen vacancies and by decreasing the amount of ASD. However, larger amount of oxygen vacancies would reduce the M_s while the better B-site ordering would improve the M_s and the spin polarization of SFMO films. Therefore, reducing the amount of ASD is essential in achieving high quality SFMO films for applications. In addition to SFMO, structural imperfections like ASD and oxygen vacancies are also important in other double perovskite materials. Hence, it is expected that these results give an indication about the magnetic behaviour also in these materials, especially in compounds like Sr_2CrReO_6 and Sr_2FeReO_6 due to their similarities in electronic structure and exchange mechanism with SFMO.

The magneto-transport properties of SFMO thin films do not follow any traditional models, but seems to be dependent on the structural imperfections and changes. The developed two spin-channel model describes the temperature dependence of resistivity quite well, including the observed low temperature upturn. The resistivity-temperature behaviour of SFMO thin films seems to be dominated by the structural defects that narrow the band gap in the majority spin channel and hence enable the thermal excitation of the electrons to the conduction band. The magnetoresistance in SFMO thin films is also dependent on these defects due to the changes in the spin polarization. In addition, the MR effect depends on the amount of low angle grain boundaries and other lattice mismatch related defects, which makes clear that the MR in SFMO thin films is a superposition of a different mechanism. Further investigations are needed to fully understand the complex magneto-transport in SFMO thin films.

Despite its high potential, there are still several issues that need to be taken into account, before SFMO can be considered for spintronic and magnetoresistive applications. Even though we have clarified the reasons for lower T_C, these results have not yet been utilized and SFMO films with high T_C have not been made. Also, the magnitude of the intrinsic magnetoresistance is still quite modest in small fields at room temperature and the growth conditions are rather demanding for the large scale fabrication. After these issues have been addressed, the potential of SFMO might be an advantage in completely new type of applications.

References

[1] J. M. D. Coey, *Magnetism and magnetic materials* (Cambridge University Press, 2010).

[2] C. Kittel, *Introduction to Solid State Physics, 8th ed.* (John Wiley & Sons, Inc, 2005).

[3] J. Crangle, *Solid State Magnetism* (Edward Arnold publishers, 1991).

[4] F. Duan and J. Guojun, *Introduction to Condensed Matter Physics, Volume 1* (World Scientific Publishing, 2005).

[5] P. F. Maldague and C. A. Kukkonen, Phys. Rev. B **19**, 6172 (1979).

[6] N. F. Mott and H. H. Wills, Proc. Roy. Soc. London **A153**, 699 (1936).

[7] N. F. Mott and H. H. Wills, Proc. Roy. Soc. London **A156**, 368 (1936).

[8] A. Fert and I. A. Campbell, Phys. Rev. Lett. **21**, 1190 (1968).

[9] M. N. Baibich *et al.*, Phys. Rev. Lett. **61**, 2472 (1988).

[10] G. Binasch, P. Grünberg, F. Saurenbach, and W. Zinn, Phys. Rev. B **39**, 4828 (1989).

[11] S. S. P. Parkin, Phys. Rev. Lett. **71**, 1641 (1993).

[12] J. Inoue, J. Magn. and Magn. Mater. **164**, 273 (1996).

[13] P. Zahn *et al.*, Phys. Rev. Lett. **80**, 4311 (1998).

[14] M. Julliere, Physics Letters **54A**, 225 (1975).

[15] A. P. Ramirez, J. Phys. Cond. Mat. **9**, 8171 (1997).

[16] P. K. Siwach, H. K. Singh, and O. N. Srivastava, J. Phys. Cond. Mat. **20**, 273207 (2008).

[17] K.-I. Kobayashi *et al.*, Nature **395**, 677 (1998).

[18] D. Sanchez *et al.*, Phys. Rev. B **65**, 104426 (2002).

[19] Y. Zhai, J. Qiao, G. Huo, and S. Han, J. Magn. and Magn. Mater. **324**, 2006 (2012).

[20] G. Y. Liu *et al.*, J. Phys. Cond. Mat. **15**, 2053 (2003).

[21] G.Y. Liu *et al.*, Journal of Alloys and Compounds **353**, 42 (2003).

[22] J. R. Hayes and A. P. Grosvenor, J. All. Comp. **537**, 323 (2012).

[23] A. Venimadhav, F. Sher, J. P. Attfield, and M. G. Blamire, J. Magn. and Magn. Mater. **269**, 101 (2004).

[24] S. Colis *et al.*, J. Appl. Phys. **98**, 033905 (2005).

[25] M. Besse *et al.*, J. Crystal Growth **241**, 448 (2002).

[26] R. P. Borges *et al.*, Thin Solid Films **429**, 5 (2003).

[27] S. R. Shinde *et al.*, J. Appl. Phys. **93**, 1605 (2003).

[28] D. Sanchez *et al.*, J. Magn. and Magn. Mater. **294**, e119 (2005).

[29] W. Westerburg, D. Reisinger, and G. Jakob, Phys. Rev. B **62**, R767 (2000).

[30] H. Asano *et al.*, Appl. Phys. Lett. **74**, 3696 (1999).

[31] C. Meneghini *et al.*, Phys. Rev. Lett. **103**, 046403 (2009).

[32] A. S. Ogale, S. B. Ogale, R. Ramesh, and T. Venkatesan, Appl. Phys. Lett. **75**, 537 (1999).

[33] D. Sánchez, M. García-Hernández, N. Auth, and G. Jakob, J. Appl. Phys. **96**, 2736 (2004).

[34] LI. Balcells *et al.*, Appl. Phys. Lett. **78**, 781 (2001).

[35] B. J. Park *et al.*, J. Magn. and Magn. Mater. **272-276**, 1851 (2004).

[36] V. N. Singh and P. Majumdar, Europhys. Lett. **94**, 47004 (2011).

[37] D. Stoeffler and S. Colis, J. Phys. Cond. Mat. **17**, 6415 (2005).

[38] D. Stoeffler and S. Colis, J. Magn. and Magn. Mater. **290-291**, 400 (2005).

[39] D. Stoeffler and S. Colis, Materials Science and Engineering B **126**, 133 (2006).

[40] T. Saha-Dasgupta and D. D. Sarma, Phys. Rev. B **64**, 064408 (2001).

[41] Z. Szotek *et al.*, Phys. Rev. B **68**, 104411 (2003).

[42] H.-T. Jeng and G. Y. Guo, Phys. Rev. B **67**, 094438 (2003).

[43] J. Lindén, T. Yamamoto, M. Karppinen, and H. Yamauchi, Appl. Phys. Lett. **76**, 2925 (2000).

[44] J. Navarro *et al.*, Phys. Rev. B **70**, 054423 (2004).

[45] T.-Y. Cai and Z.-Y. Li, J. Phys. Cond. Mat. **16**, 3737 (2004).

[46] M. Hoffmann *et al.*, arXiv:1504.02629 (2015).

[47] J. Raittila *et al.*, J. Phys. Chem. Solids **67**, 1712 (2006).

[48] T. Suominen *et al.*, J. Magn. and Magn. Mater. **309**, 278 (2007).

[49] Y. Tomioka *et al.*, Phys. Rev. B **61**, 422 (2000).

[50] A. di Trolio *et al.*, J. Appl. Phys. **100**, 013907 (2006).

[51] T. Manako *et al.*, Appl. Phys. Lett. **74**, 2215 (1999).

[52] T. Kobayashi *et al.*, Jpn. J. Appl. Phys. **27**, 1880 (1988).

[53] P. Raychaudhuri, T.K. Nath, A. K. Nigam, and R. Pinto, J. Appl. Phys. **84**, 2048 (1998).

[54] P. K. Muduli, R. C. Budhani, D. Topwal, and D. D. Sarma, J. Phys. Conf. Ser. **150**, 042132 (2009).

[55] T.H. Kim, M. Uehara, S-W. Cheong, and S. Lee, Appl. Phys. Lett. **74**, 1737 (1999).

[56] S. Sharma *et al.*, Appl. Phys. Lett. **83**, 2384 (2003).

[57] D. Niebieskikwiat, A. Caneiro, R. D. Sanchez, and J. Fontcuberta, Phys. Rev. B **64**, 180406 (2001).

[58] T.T. Fang, Phys. Rev. B **71**, 064401 (2005).

[59] J. Navarro *et al.*, J. Phys: Condens. Matter **13**, 8481 (2001).

[60] D.D. Sarma *et al.*, Solid State Communications **114**, 465 (2000).

[61] J. H. Song, J.-H. Park, and Y. H. Jeong, J. Appl. Phys. **97**, 46105 (2005).

[62] R. Boucher, J. Magn. and Magn. Mater. **301**, 251 (2006).

[63] M. Retuerto *et al.*, Appl. Phys. Lett. **85**, 266 (2004).

[64] X. H. Li *et al.*, Solid State. Commun. **145**, 98 (2008).

[65] C. L. Yuan *et al.*, Appl. Phys. Lett. **75**, 3853 (1999).

[66] W.H. Song *et al.*, J. Appl. Phys. **89**, 7678 (2001).

[67] C. L. Yuan *et al.*, Physica B **334**, 408 (2003).

[68] Y. H. Huang, J. Lindén, H. Yamauchi, and M. Karppinen, Appl. Phys. Lett. **86**, 072510 (2005).

[69] J. Santiso, A. Figueras, and J. Fraxedas, Surf. Interface Anal. **33**, 676 (2002).

[70] T. Fix *et al.*, J. Appl. Phys. **97**, 024907 (2005).

[71] D. Kumar and D. Kaur, Physica B **405**, 3259 (2010).

[72] T. Yamaguchi, H. Suwaki, K. Kikuta, and S. Hirano, Solid State Communications **133**, 71 (2005).

[73] H. Suwaki *et al.*, J. Magn. and Magn. Mater. **295**, 230 (2005).

[74] X. B. Zhu *et al.*, Materials Letters **59**, 2366 (2005).

[75] J. Rager *et al.*, Appl. Phys. Lett. **81**, 5003 (2002).

[76] R. Boucher, Journal of Physics and Chemistry of Solids **66**, 1020 (2005).

[77] A. J. Hauser *et al.*, Phys. Rev. B **83**, 014407 (2011).

[78] J. Als-Nielsen and D. McMorrow, *Elements of modern x-ray physics* (Wiley, 2010).

[79] J. B. Nelson and D. P. Riley, Proc. Phys. Soc. **57**, 160 (1945).

[80] M. Birkholz, *Thin Film Analysis by X-ray Scattering* (Wiley-VCH, 2006).

[81] Ll. Balcells *et al.*, Appl. Phys. Lett. **78**, 781 (2001).

[82] J. Rodriguez-Carvajal, Abstracts of the Satellite Meeting on Powder Diffraction of the XV Congress of the IUCr 127 (1990).

[83] J. Rodriguez-Carvajal, Physica B **192**, 55 (1993).

[84] F. Schaefers, M. Mertin, and M. Gorgoi, Rev. Sci. Instrum. **78**, 123102 (2007).

[85] T. Suominen, J. Raittila, and P. Paturi, Thin Solid Films **517**, 5793 (2009).

[86] A. Venimadhav, M. E. Vickers, and M. G. Blamire, Solid State Communications **130**, 631 (2004).

[87] S. Wang *et al.*, Appl. Phys. Lett. **88**, 121912 (2006).

[88] H. Jalili, N. F. Heinig, and K. T. Leung, Phys. Rev. B **79**, 174427 (2009).

[89] B. Aguilar, O. Navarro, and M. Avignon, Microelectronics Journal **39**, 560 (2008).

[90] T. Namikawa *et al.*, IEEE T. Magn. **35**, 2850 (1999).

[91] Chang Seop Hong, Wan Seop Kim, and Nam Hwi Hur, Solid Stata Communications **120**, 359 (2001).

[92] L. S. Hsu, C. J. Liu, T. W. Wu, and D. Luca, Journal of Optoelectronics and Advanced Materials **5**, 409 (2003).

[93] S. Hu *et al.*, AIP Advances **4**, 067109 (2014).

[94] T. Fix *et al.*, J. Appl. Phys. **98**, 023712 (2005).

[95] H. Jalili, N. F. Heinig, and K. T. Leung, J. Chem. Phys **132**, 204701 (2010).

[96] H. Jalili, N. F. Heinig, and K. T. Leung, J. Appl. Phys. **105**, 034305 (2009).

[97] W.-J. Ji *et al.*, Solid State Commun. **163**, 28 (2013).

[98] L. Ranno, A. Llobet, R. Tiron, and E. Favre-Nicolin, Applied Surface Science **188**, 170 (2002).

[99] P. X. Zhang, H. Zhang, L. M. Cha, and H.-U. Habermeier, Physica B **327**, 257 (2003).

[100] S. Nakamura and K. Oikawa, J. Phys. Soc. Jpn. **72**, 3123 (2003).

[101] Z. Wang, Y. Tian, and Y. Li, J. Power Sources **196**, 6104 (2011).

[102] H. Deniz *et al.*, J. Mater. Sci. **50**, 3131 (2015).

[103] Y. Moritomo *et al.*, Jpn. J. Appl. Phys. **40**, 672 (2001).

[104] Y. H. Huang, M. Karppinen, H. Yamauchi, and J. B. Goodenough, Phys. Rev. B **73**, 104408 (2006).

[105] R. Kircheisen and J. Töpfer, Journal of Solid State Chemistry **185**, 76 (2012).

[106] J. Töpfer, R. Kircheisen, and S. Barth, J. Appl. Phys. **105**, 07D712 (2009).

[107] Q. Zhang *et al.*, J. Alloys Compd. **649**, 1151 (2015).

[108] R. P. Panguluri *et al.*, Appl. Phys. Lett. **94**, 012501 (2009).

[109] H. Wu *et al.*, Solid State Commun. **177**, 57 (2014).

[110] L. Lutterotti, Material Analysis Using Diffraction 2.33 [computer program] `http://www.ing.unitn.it/~maud/`, accessed 7th May 2015 (1997-2011).

[111] V. R. Galakhov *et al.*, J. Phys. Chem. C **114**, 5154 (2010).

[112] H. Tan *et al.*, Appl. Mater. Interfaces **6**, 19184 (2014).

[113] J. M. De Teresa *et al.*, Phys. Rev. B **54**, 1187 (1996).

[114] G. J. Snyder *et al.*, Phys. Rev. B **53**, 14434 (1996).

[115] A. Urushibara *et al.*, Phys. Rev. B **51**, 14103 (1995).

[116] Li Pi, Lei Zheng, and Yuheng Zhang, Phys. Rev. B **61**, 8917 (2000).

[117] D. D. Sarma *et al.*, Phys. Rev. Lett. **85**, 2549 (2000).

[118] V. Kanchana, G. Vaitheeswaran, M. Alouani, and A. Delin, Phys. Rev. B **75**, 220404 (2007).

[119] B. García-Landa *et al.*, Solid state commun. **110**, 435 (1999).

[120] P. A. Lee and T.V. Ramakrishnan, Rev. Mod. Phys. **57**, 287 (1985).

[121] S. Majumdar, H. S. Majumdar, D. Tobjörk, and R. Österbacka, Phys. Status Solidi A **206**, 2198 (2009).

[122] S. Majumdar, H. Huhtinen, H.S. Majumdar, and P. Paturi, J. Alloys Compd. **512**, 332 (2012).